

Technical University of Munich  
School of Natural Sciences



Master's Thesis in Nuclear, Particle and Astrophysics

# Data Quality and Neutrino Mass Sensitivity of the 6th to 9th KATRIN campaigns

Datenqualität und Neutrinomassensensitivität der 6. bis 9. KATRIN  
Kampagnen

Jan Plößner

02 September 2024

Primary reviewer: Prof. S. Mertens  
Secondary reviewer: Prof. T. Lasserre  
Supervisors: A. Schwemmer, X. Stribl, Dr. C. Wiesinger

# Abstract

The neutrino mass is a key parameter in particle physics and cosmology, but its value is still unknown. The KARlsruhe TRItium Neutrino (KATRIN) experiment utilizes the  $\beta$ -decay of tritium to measure the effective electron anti-neutrino mass  $m_\nu$ . KATRIN will take data until the end of 2025 with a projected final sensitivity of  $m_\nu < 0.3 \text{ eV}$  (90 % C.L.). The latest result is an upper limit of  $m_\nu < 0.45 \text{ eV}$  (90 % C.L.). It is based on data from the first five measurement campaigns, corresponding to approximately 20 % of the final statistics.

Within this thesis, the data quality of the following four, yet blinded, KATRIN measurement campaigns is investigated, and the neutrino mass sensitivity of these campaigns is obtained. The implementation of new features in the data monitoring allows following the statistics collection and ensures an efficient continuation of the KATRIN measurement.

To ensure the quality of the data, the temporal stability of the fit parameters was studied by individual fits to all 1524 measurement runs. The spatial behaviour was investigated by fits to data that was recorded by different sections of the detector. No problematic outliers were found. The first step of the neutrino mass inference based on the 6th to 9th KATRIN campaigns was initiated by fits on simulated data. This allowed to determine the  $m_\nu^2$  sensitivity of these four campaigns. The total  $1\text{-}\sigma$  uncertainties lie between 0.170 and 0.212eV<sup>2</sup>. The systematic uncertainties reach from 0.048 to 0.75eV<sup>2</sup>. The dominant systematic effects are the gas density of the source, the energy loss of the electrons and effects related to the source plasma, which are to be improved for the final KATRIN result. The estimated combined sensitivity of the first nine campaigns is  $m_\nu < 0.39 \text{ eV}$  (90 % C.L.), which brings KATRIN closer to its final sensitivity.



# Contents

<b>Abstract</b>	<b>iii</b>
<b>1 Neutrino Physics</b>	<b>1</b>
1.1 Discovery of the neutrino . . . . .	1
1.2 Neutrinos in the Standard Model . . . . .	2
1.3 Neutrino oscillations . . . . .	3
1.4 Determination of the absolute neutrino masses . . . . .	4
1.4.1 Cosmology . . . . .	4
1.4.2 Neutrinoless double $\beta$ -decay ( $0\nu\beta\beta$ ) . . . . .	4
1.4.3 Kinematics of the $\beta$ -decay . . . . .	5
<b>2 The KATRIN Experiment</b>	<b>7</b>
2.1 Experimental setup . . . . .	7
2.1.1 Rear section . . . . .	8
2.1.2 Windowless gaseous tritium source . . . . .	8
2.1.3 Transport and pumping section . . . . .	9
2.1.4 Pre- and main spectrometer . . . . .	9
2.1.5 Detector section . . . . .	12
2.2 Modelling of the $\beta$ -decay spectrum . . . . .	12
2.2.1 Final states distribution . . . . .	13
2.2.2 Doppler effect . . . . .	13
2.2.3 Experimental response function . . . . .	14
2.2.4 Model of the expected rate . . . . .	17
2.3 Systematic uncertainties . . . . .	19
2.3.1 Source-related uncertainties . . . . .	19
2.3.2 Background-related uncertainties . . . . .	22
2.3.3 Electromagnetic-fields-related uncertainties . . . . .	23
2.3.4 Detector-related uncertainties . . . . .	24
2.3.5 FSD-related uncertainties . . . . .	25
2.4 Analysis strategies . . . . .	25
2.4.1 Maximum likelihood method . . . . .	26
2.4.2 Data combination . . . . .	27
2.4.3 Treatment of systematic effects . . . . .	29
2.4.4 Software . . . . .	31

2.5	Current KATRIN neutrino mass result . . . . .	32
<b>3</b>	<b>Data Monitoring</b>	<b>35</b>
<b>4</b>	<b>Analysis of the 6th to 9th KATRIN campaigns</b>	<b>39</b>
4.1	Data selection . . . . .	39
4.1.1	$\beta$ -scan selection . . . . .	39
4.1.2	Pixel and patch selection . . . . .	42
4.2	Systematic input parameters . . . . .	46
4.3	Data quality . . . . .	47
4.3.1	Fit parameter stability . . . . .	48
4.3.2	Scanning directions . . . . .	52
4.4	Neutrino mass analysis . . . . .	54
4.4.1	Blinding strategy . . . . .	55
4.4.2	Sensitivity results . . . . .	57
<b>5</b>	<b>Conclusion and Outlook</b>	<b>63</b>
	<b>Bibliography</b>	<b>65</b>
	<b>Appendix</b>	<b>71</b>

# Chapter 1

## Neutrino Physics

Neutrinos play a key role in answering some of the open questions in physics, e.g. the origin of the neutrino mass. This chapter gives a brief introduction to the history of neutrinos, starting with their postulation and discovery. It provides information about the current understanding of the neutrino properties and oscillations. Finally, it describes experimental approaches to determine the neutrino mass.

### 1.1 Discovery of the neutrino

Wolfgang Pauli first postulated the neutrino in 1930 to explain the observed continuous energy spectrum of the  $\beta$ -decay [1]. Without the addition of a new neutral spin- $\frac{1}{2}$  particle, the underlying process was thought to be a two-body decay, where the electron should receive a constant amount of energy and create a corresponding peak-like signal (see figure 1.1). The neutrino carries away a part of the available energy of the  $\beta$ -decay, which leads to the observed spectrum.

More than 20 years later, in 1956, Clyde Cowan and Fred Reines discovered the neutrino with their project "Poltergeist" using the inverse  $\beta^+$ -decay [2]:



In the experiment an electron anti-neutrino  $\bar{\nu}_e$  from a reactor interacts with a proton  $p$  in water and produces a neutron  $n$  and a positron  $e^+$ . The positron immediately annihilates with an electron and emits two characteristic 511 keV photons. The neutron thermalizes and is captured by Cadmium, which is dissolved in water. In the de-excitation of  $^{109}\text{Cd}^*$ , photons with a total energy of a few MeV are released with a delay of a few  $\mu\text{s}$ . The emitted photons from the annihilation and the de-excitation are detected with scintillators and photomultiplier tubes (PMTs). With this clear double pulse signal, the inverse  $\beta^+$ -decay could be detected and distinguished from background events.

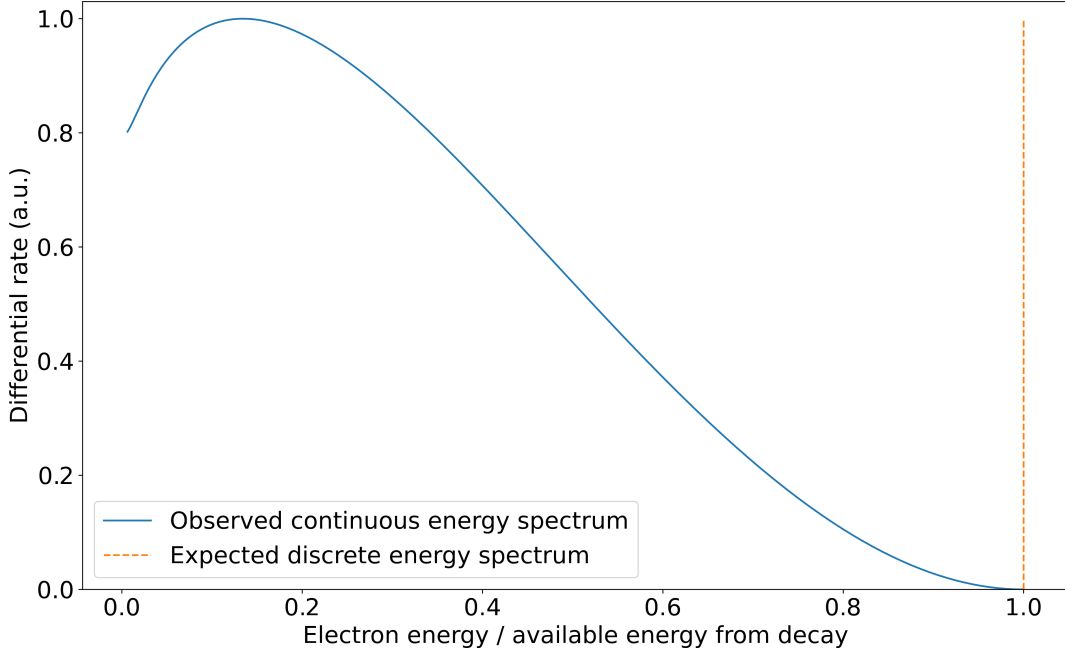


Figure 1.1: Illustration of the differential energy spectrum of  $\beta$ -decay electrons. The orange dashed line shows the expected discrete spectrum due to momentum and energy conservation of a two-body decay. The blue line shows the observed continuous spectrum, which can be explained by an additional neutral spin- $\frac{1}{2}$  particle, the neutrino.

## 1.2 Neutrinos in the Standard Model

Today, the neutrino is well embedded in the Standard Model (SM) of particle physics: It is a weakly interacting fermion with no electric charge [3]. For every negatively charged lepton ( $e^-$ ,  $\mu^-$ ,  $\tau^-$ ), a neutrino flavour is introduced ( $\nu_e$ ,  $\nu_\mu$ ,  $\nu_\tau$ ) and has been measured [2, 4, 5]. Together, they build the three lepton families

$$\begin{pmatrix} \nu_e \\ e^- \end{pmatrix} \begin{pmatrix} \nu_\mu \\ \mu^- \end{pmatrix} \begin{pmatrix} \nu_\tau \\ \tau^- \end{pmatrix}. \quad (1.2)$$

However, there are some open questions related to the neutrino, e.g. the origin of its mass, which the SM can not explain. One of the first evidence for physics beyond the SM was the observation of neutrino oscillations [6, 7] and the consequence of at least two non-zero neutrino masses. This will be explained in the next section.

### 1.3 Neutrino oscillations

The first hint for neutrino oscillations was the so-called solar neutrino problem, where fewer electron neutrinos  $\nu_e$  from the sun were measured via the inverse  $\beta^-$ -decay of  $^{37}\text{Cl}$  than predicted by the solar models [8, 9]. A similar observation appeared for atmospheric neutrinos: A lower ratio of muon neutrinos  $\nu_\mu$  to electron neutrinos  $\nu_e$  from the atmosphere was measured with a water Cherenkov detector than the predicted ratio of 2:1 [10]. A first conclusive hint of neutrino oscillations was provided by the Super-Kamiokande experiment, which observed a deficit of muon neutrinos dependent on the zenith angle [6]. The final experimental confirmation for neutrino oscillations was provided by the SNO experiment [7]. The total neutrino flux from the sun could be determined by measuring the neutral current reactions of all neutrino flavours with deuterium, where the  $Z^0$ -boson acts as mediator. The lack of electron neutrinos was still visible, but the total neutrino flux agreed with the solar models. Consequently, the concept of neutrino oscillations has been developed, which will be explained in the following.

The three neutrino mass eigenstates  $|\nu_1\rangle$ ,  $|\nu_2\rangle$  and  $|\nu_3\rangle$  with a defined but yet unknown mass are different from the three flavour eigenstates  $|\nu_e\rangle$ ,  $|\nu_\mu\rangle$  and  $|\nu_\tau\rangle$ . More precisely, the flavour eigenstates can be expressed as mutually orthogonal linear combinations of the three mass eigenstates [3]. This is described by the unitary PMNS matrix  $\mathbf{U}$  named after Pontecorvo, Maki, Nakagawa and Sakata, who first considered the idea of neutrino oscillations [11–13]:

$$\begin{pmatrix} |\nu_e\rangle \\ |\nu_\mu\rangle \\ |\nu_\tau\rangle \end{pmatrix} = \begin{pmatrix} U_{e1} & U_{e2} & U_{e3} \\ U_{\mu1} & U_{\mu2} & U_{\mu3} \\ U_{\tau1} & U_{\tau2} & U_{\tau3} \end{pmatrix} \begin{pmatrix} |\nu_1\rangle \\ |\nu_2\rangle \\ |\nu_3\rangle \end{pmatrix} \quad (1.3)$$

The PMNS matrix can be parameterized by three mixing angles and up to three phases, where only the one related to charge-parity (CP) violations is relevant for neutrino oscillations. The other two phases are present in the Majorana case, i.e. if the neutrino is its own anti-particle, and do not affect oscillations [14]. For a clearer introduction to neutrino oscillations, the simplified case of two different neutrino flavours  $|\nu_\alpha\rangle$  and  $|\nu_\beta\rangle$  is discussed in the following. Equation 1.3 reduces to

$$\begin{pmatrix} |\nu_\alpha\rangle \\ |\nu_\beta\rangle \end{pmatrix} = \begin{pmatrix} \cos(\theta) & \sin(\theta) \\ -\sin(\theta) & \cos(\theta) \end{pmatrix} \begin{pmatrix} |\nu_1\rangle \\ |\nu_2\rangle \end{pmatrix} \quad (1.4)$$

with one mixing angle  $\theta$  [3].

After creating a neutrino in a flavour eigenstate, e.g.  $|\nu_\alpha\rangle$  via the weak interaction, the mass eigenstates propagate with different velocities. This is described by the wave function

$$|\nu_\alpha(t)\rangle = \cos(\theta) \cdot e^{-iE_{\nu_1}t/\hbar} |\nu_1\rangle + \sin(\theta) \cdot e^{-iE_{\nu_2}t/\hbar} |\nu_2\rangle \quad (1.5)$$

with the time after creation  $t$ , the neutrino energies  $E_{\nu_i}$  ( $i = 1, 2$ ) and the reduced Planck constant  $\hbar$ . The probability  $P_{\nu_\alpha \rightarrow \nu_\beta}$  of the neutrino in the flavour eigenstate  $|\nu_\alpha\rangle$  to be found in the flavour eigenstate  $|\nu_\beta\rangle$  is under relativistic approximation

$$P_{\nu_\alpha \rightarrow \nu_\beta} = \sin^2(2\theta) \sin^2\left(\frac{1}{4} \frac{\Delta m_{21}^2 c^4 L}{\hbar c pc}\right) \quad (1.6)$$

with the difference of the squared masses  $\Delta m_{21}^2 = m_{\nu_2}^2 - m_{\nu_1}^2$ , the speed of light  $c$ , the travelled distance  $L$  and the momentum of the neutrino  $p$  [3]. With equation 1.6, it is clear that neutrino oscillations are only possible if  $\Delta m_{21}$  and  $\theta$  are not zero. Latter means that the flavour eigenstates are not equivalent to the mass eigenstates (see equation 1.4). The former implies, for the case of three different neutrino flavours, that at least two of the neutrino masses are not zero.

## 1.4 Determination of the absolute neutrino masses

Since neutrino oscillation experiments are only sensitive to the differences of the neutrino masses (see equation 1.6), other approaches are needed to measure the absolute neutrino mass scale.

### 1.4.1 Cosmology

In the early universe, neutrinos constituted  $\sim 40\%$  of the total energy and their physical properties greatly impacted both the formation and evolution of structure in the universe. Via the study of the cosmic microwave background (CMB), the so-called baryonic acoustic oscillations (BAO) and large-scale structures (LSS) in the universe, the sum of the neutrino mass eigenstates  $m_\Sigma = \sum_{i=1}^3 m_i$  is accessible [15, 16]. The current best limit is  $m_\Sigma < 0.072 \text{ eV}$  at 95% confidence level (C.L.) provided by the DESI collaboration [17], combining their data with the observations of the Planck satellite [18] and using a flat positive prior on  $m_\Sigma$ . This determination method is dependent on the cosmological model.

### 1.4.2 Neutrinoless double $\beta$ -decay ( $0\nu\beta\beta$ )

A different idea is to determine the coherent sum of the neutrino masses weighted by their squared electron neutrino contribution  $m_{\beta\beta} = \left| \sum_{i=1}^3 U_{ei}^2 m_i \right|$  via measuring the half-life  $T_{1/2}$  of the neutrinoless double  $\beta$ -decay of a suitable isotope [19]. This is only possible if the neutrino is its own anti-particle, a so-called Majorana particle.  $T_{1/2}$  and  $m_{\beta\beta}$  are connected via the relation

$$\frac{1}{T_{1/2}} = G^{0\nu} |M^{0\nu}|^2 m_{\beta\beta}^2 \quad (1.7)$$

with the phase-space factor  $G^{0\nu}$  and the nuclear matrix element  $M^{0\nu}$ . The currently best limits on  $m_{\beta\beta}$  are  $0.079 - 0.180$  eV (90 % C.L.) for  $^{76}\text{Ge}$  [20],  $0.070 - 0.240$  eV (90 % C.L.) for  $^{130}\text{Te}$  [21], and  $0.028 - 0.122$  eV (90 % C.L.) for  $^{136}\text{Xe}$  [22]. These limits are only valid if the neutrino is a Majorana particle. The different nuclear matrix element calculations dominate the uncertainties of the results.

### 1.4.3 Kinematics of the $\beta$ -decay

One of the most direct ways to measure the absolute mass of the neutrino is via the kinematics of the  $\beta$ -decay [23]. It does not depend on the nature of neutrinos or the cosmological model.



Here, a neutron of the radioactive nucleus X decays into a proton, creating the daughter nucleus Y and emitting an electron  $e^-$  and an electron anti-neutrino  $\bar{\nu}_e$ . During this process, the surplus energy  $Q$  is released and shared between the decay products. While the daughter nucleus gets the recoil energy  $E_{\text{rec}}$ , the endpoint energy  $E_0$  is shared between the electron ( $E$ ) and the anti-neutrino ( $E_\nu$ ):

$$E_0 = Q - E_{\text{rec}} = E + E_\nu. \quad (1.9)$$

If the neutrino is massless,  $E_0$  would be the maximum energy of an electron produced in the decay. With a non-zero mass, the neutrino always carries away a part of the endpoint energy  $E_0$ , which influences the differential rate  $\frac{d\Gamma}{dE}$  of the  $\beta$ -decay electrons:

$$\begin{aligned} \frac{d\Gamma}{dE}(E) = & \frac{G_F^2 \cos^2(\theta_C)}{2\pi^3} \cdot |M_{\text{nuc}}|^2 \cdot F(Z', E) \cdot p \\ & \cdot (E + m_e) \cdot (E_0 - E) \cdot \sqrt{(E_0 - E)^2 - m_\nu^2} \cdot \Theta(E_0 - E - m_\nu) \end{aligned} \quad (1.10)$$

with the Fermi constant  $G_F$ , the Cabibbo angle  $\theta_C$ , the nuclear matrix element  $M_{\text{nuc}}$ , the proton number of the daughter nucleus  $Z'$ , the Fermi function  $F(Z', E)$ , the momentum of the electron  $p$  and the electron mass  $m_e$ . The incoherent sum of the neutrino masses, also called effective (electron anti-)neutrino mass, is

$$m_\nu = \sqrt{\sum_{i=1}^3 |U_{ei}|^2 m_i^2}. \quad (1.11)$$

The Heaviside function  $\Theta$  in equation 1.10 ensures energy conservation.

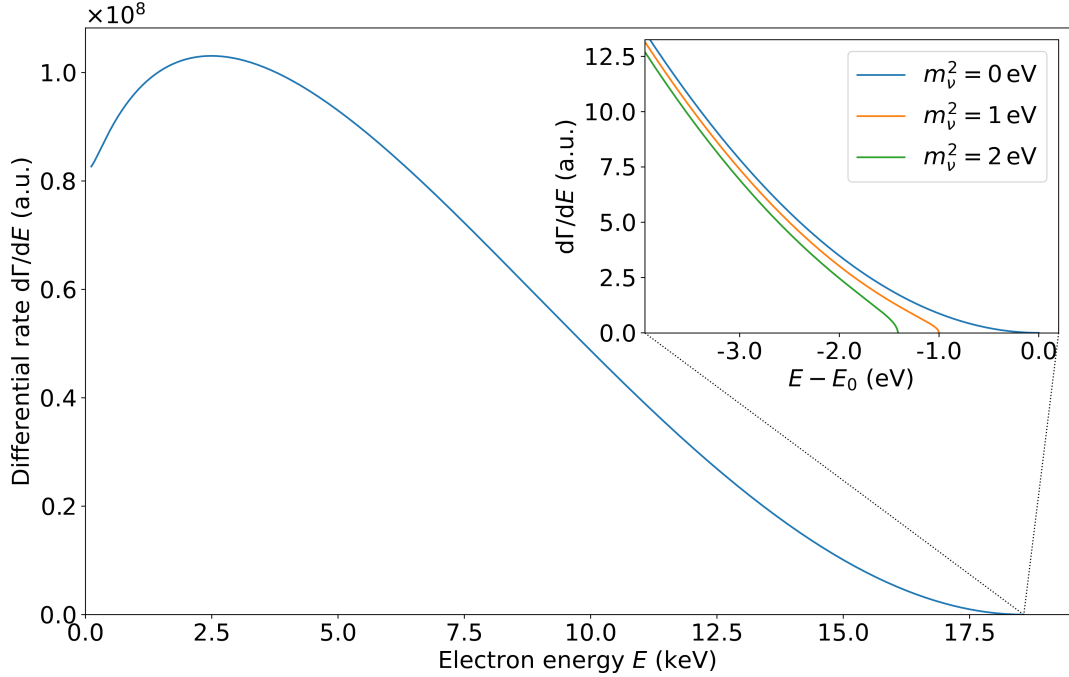


Figure 1.2: Differential rate  $\frac{d\Gamma}{dE}$  of tritium  $\beta$ -decay electrons as a function of their energy  $E$ . In the endpoint  $E_0$  region, the impact of a non-zero effective neutrino mass  $m_\nu$  shows itself as a spectral distortion and a shift of the maximum electron energy to lower values for higher masses.

Figure 1.2 shows the differential tritium  $\beta$ -decay spectrum described by equation 1.10 and the impact of a non-zero effective electron anti-neutrino mass  $m_\nu$ : A distortion of the spectrum in the endpoint region and a shift of the maximum electron energy to lower values as the effective neutrino mass increases. The precise determination of the shift is experimentally very challenging due to the tiny fraction of the decays happening in the endpoint region as indicated in figure 1.2 and the energy resolution needed to distinguish this signature. Direct neutrino mass experiments, therefore, use high activity sources of  $\beta$ -decay electrons coupled with high energy resolution detection methods to determine  $m_\nu$  via the distortion of the spectrum.

The Karlsruhe TRItium Neutrino (KATRIN) experiment [24] - which will be explained in more detail in the following chapter - currently sets the best limit on the effective electron anti-neutrino mass with  $m_\nu < 0.45$  eV (90% C.L.) [25].

## Chapter 2

# The KATRIN Experiment

The Karlsruhe TRITium Neutrino (KATRIN) experiment [24] is located at the Karlsruhe Institute of Technology (KIT) [26] and uses the infrastructure of the Tritium Laboratory Karlsruhe (TLK) [27]. It has been taking data since 2018 [28]. As the successor of the experiments in Mainz [29] and Troitsk [30], it aims to measure the effective electron anti-neutrino mass  $m_\nu$  (equation 1.11) via the kinematics of the  $\beta$ -decay (see section 1.4) of tritium with a projected final sensitivity of  $m_\nu < 0.3$  eV [25].

This chapter describes the experimental setup of the KATRIN experiment [28], derives the model of the  $\beta$ -decay spectrum [31], introduces the sources of systematic uncertainties and explains the analysis strategies being used [32].

### 2.1 Experimental setup

There are challenges a direct neutrino mass search experiment has to tackle since the neutrino mass only impacts a very limited region of the  $\beta$ -decay spectrum as shown

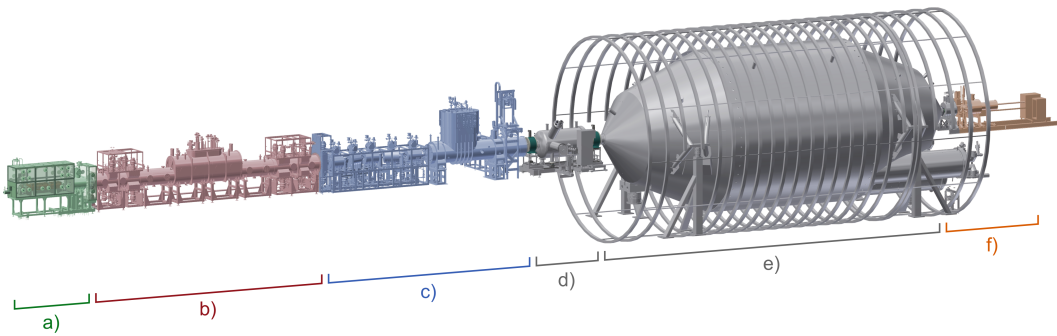


Figure 2.1: Schematic view of the 70 m long KATRIN experimental setup. a) Rear Section (RS) b) Windowless Gaseous Tritium Source (WGTS) c) Transport and Pumping Section (TPS) d) Pre-spectrometer (PS) e) Main Spectrometer (MS) f) Detector section (DS). Figure provided by Leonard Köllenberger.

in figure 1.2. The experiment needs an excellent energy resolution and a source with large enough activity to be able to measure the spectral distortion caused by the non-zero neutrino mass. The KATRIN experiment masters these challenges with its 70 m long beamline, shown in figure 2.1. It consists of six components, which will be explained in more detail in the following sections.

- a) Rear Section (RS)
- b) Windowless Gaseous Tritium Source (WGTS)
- c) Transport and Pumping Section (TPS)
- d) Pre-spectrometer (PS)
- e) Main Spectrometer (MS)
- f) Detector Section (DS)

### 2.1.1 Rear section

The rear section (RS) consists of the rear wall (RW), which is a gold-coated stainless steel disk with an outer diameter of 145 mm [28], an electron gun (e-gun) for monitoring and calibration purposes, and a superconducting magnet to guide the e-gun electrons into the windowless gaseous tritium source (see next section). The RS enables the monitoring of important operation parameters, e.g. the source gas composition and activity.

With the RW, the plasma of the tritium source can be manipulated in order to create a homogeneous starting potential for the  $\beta$ -electrons [28]. This will be explained in more detail in section 2.3.1. To do so, a bias voltage of up to  $\pm 500$  V can be applied to the RW.

### 2.1.2 Windowless gaseous tritium source

As a  $\beta$ -decay source, the KATRIN experiment uses molecular tritium  $T_2$  in its gaseous form. It has a few advantages over other isotopes for the direct neutrino mass search [23]:

- It has the second lowest endpoint energy of all  $\beta$ -decay isotopes with  $E_0 \approx 18.6$  keV [33]. This leads to relatively more counts in the endpoint region where the shape distortion of the energy spectrum through the non-zero neutrino mass is most prominent (see figure 1.2).

- The  $\beta$ -decay of tritium is a super-allowed process with a rather short half-life of  $T_{1/2} = 12.3$  a. This allows very high source activity of the KATRIN experiment and leads to a nuclear matrix element (in equation 1.10) independent of the electron energy.
- It is the simplest molecule allowing quantitative calculation of its final states distribution (compare section 2.2.1).
- To reduce the broadening of the  $\beta$ -spectrum caused by the Doppler effect (compare section 2.2.2), the windowless gaseous tritium source (WGTS) is operated at low temperatures ( $< 100$  K). Molecular tritium is still in its gaseous state at these temperatures, which avoids complicated solid-state effects [34].

The molecular tritium gas with an activity of up to  $10^{11}$  Bq is streaming through a 10 m long source tube with a diameter of 90 mm [28]. Half of the isotropically emitted  $\beta$ -electrons are adiabatically guided from the WGTS downstream towards the detector (see section 2.1.5) by a homogeneous magnetic field of up to  $3.6 \text{ T}^1$  generated by superconducting solenoids. The other half travels upstream to the rear wall, where they get absorbed and neutralized. From both ends of the windowless source tube, tritium molecules are pumped away, and treated tritium is continuously injected in the middle of the tube to maintain a high purity of the source. This closed loop system processes up to 40 g of pure tritium per day (see [35] for more details).

### 2.1.3 Transport and pumping section

Through the transport and pumping section (TPS), the  $\beta$ -electrons from the tritium source are guided adiabatically to the spectrometer section (see next section) by twelve magnets. To keep the background rate, originating from tritium contamination of the main spectrometer below  $10^{-3}$  cps, the tritium flow rate between the WGTS and the spectrometer section is reduced by more than 12 orders of magnitude [28]. This is achieved by a combination of differential and cryogenic pumping.

### 2.1.4 Pre- and main spectrometer

There are two spectrometers installed in the KATRIN beamline (see figure 2.1), the pre- (PS) and the main spectrometer (MS). Both act as a so-called MAC-E (magnetic

---

<sup>1</sup>In the standard setting the magnetic field of the source has a strength of around 2.5 T [28].

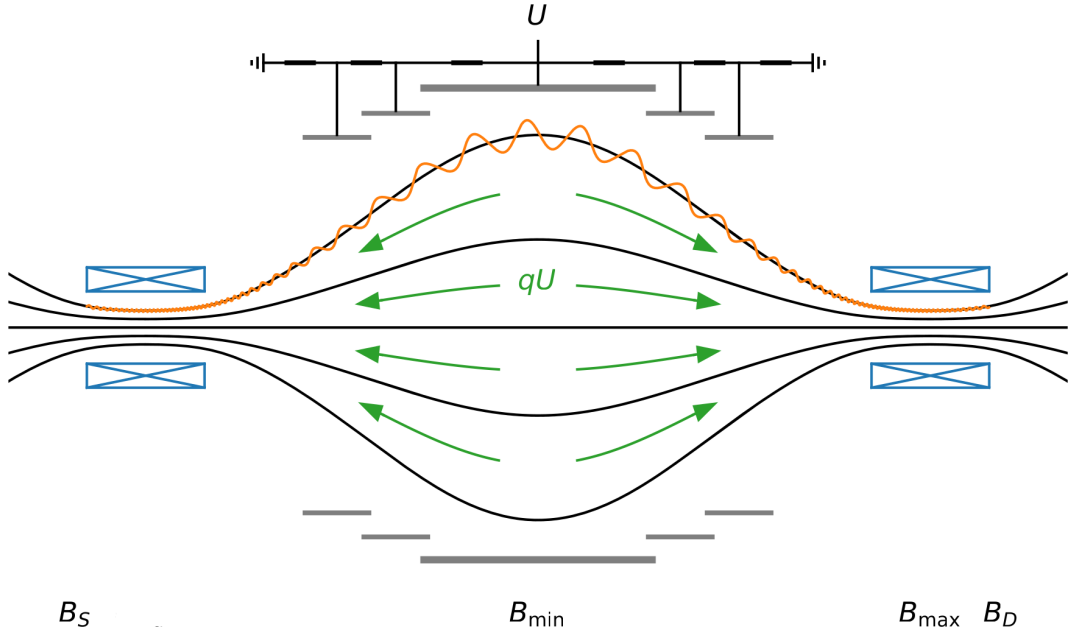


Figure 2.2: MAC-E (magnetic adiabatic collimation with electrostatic) filter working principle of the KATRIN spectrometer. Electrons (orange line) from the source (with  $B_S$ ) are guided along the magnetic field lines (black) towards the spectrometer. They have to overcome the retarding potential  $qU$  (green arrows) in the analyzing plane (with  $B_{\min}$ ) in order to reach the detector (with  $B_D$ ). The retarding potential is only sensitive to the longitudinal component of the electron energy  $E_{\parallel}$ . The magnetic gradient force, which occurs due to the depicted magnet field configuration, transforms the transversal energy component into the longitudinal one. To reflect  $\beta$ -electrons with very large starting angles, the maximum magnetic field  $B_{\max}$  is set between the analyzing plane and the detector. Figure adapted from [34].

adiabatic collimation with electrostatic) filter<sup>2</sup>. This principle is depicted in figure 2.2.

Half of the  $\beta$ -electrons emitted isotropically by the tritium source are transported adiabatically by a magnetic field towards the so-called analyzing plane in the MS. There they have to overcome the retarding potential  $qU$  ( $q = -1e$  with the electric charge of the electron  $e$ ). Only electrons with greater kinetic energy than this retarding energy get re-accelerated towards the detector by a post acceleration electrode

<sup>2</sup>The PS was used as a pre-filter for low energy electrons to reduce the electron flux into the main spectrometer. But because the combination of two high-voltage MAC-E filters in series leads to the formation of a so-called Penning trap, which causes an additional background, the PS is no longer operated at high voltages [25].

(see next section) and get counted. Hence, the spectrometer acts as a high-pass filter for the electron energy. The retarding voltage  $U$  applied to the spectrometer can be varied. This results in a measurement of the integral spectrum of the tritium  $\beta$ -decay.

The retarding potential is only sensitive to the longitudinal energy component of the electrons  $E_{\parallel}$ . Thus, it is crucial that in the analyzing plane, the total kinetic energy of the electrons is collimated into the longitudinal direction:

$$E_{\text{kin}} = E_{\parallel} + E_{\perp} \approx E_{\parallel}. \quad (2.1)$$

The residual transversal component  $E_{\perp}$  defines the energy resolution  $\Delta E$  of the spectrometer. Defining the electron pitch angle  $\theta$ , the different components can be written as  $E_{\parallel} = E \cos^2(\theta)$  and  $E_{\perp} = E \sin^2(\theta)$ .

To assure equation 2.1, the momenta of the electrons are collimated magnetically and adiabatically via the inverse magnetic mirror effect [36–38]. The electrons perform a cyclotron motion while travelling along the magnetic field lines. Including relativistic effects, the value of the expression

$$\frac{p_{\perp}^2}{B} = \frac{E_{\perp} \cdot (\gamma + 1) \cdot m_e}{B} = \text{const.} \quad (2.2)$$

is conserved (with the transversal momentum of the electron  $p_{\perp}$ , the changing magnetic field  $B$  and the relativistic gamma factor  $\gamma = \frac{E+m_e}{m_e}$ ).

The  $\beta$ -electrons are emitted in a region with a high magnetic field ( $B_S \approx 2.5$  T). While they are guided to the analyzing plane, the field strength drops by several orders of magnitude ( $B_{\text{min}} = \mathcal{O}(10^{-3}$  T)) and the transversal energy component is transformed into the longitudinal one by the magnetic gradient force (see equation 2.2). The electrons which overcome the retarding potential are focused onto the detector with an again increased magnetic field ( $B_D \approx 2.4$  T).

$\beta$ -electrons emitted with very large angles travel longer distances before they leave the source and, therefore, scatter more often on residual tritium molecules (compare section 2.2.3). To reflect these electrons, the maximum magnetic field  $B_{\text{max}} \approx 4.2$  T is set between the analyzing plane ( $B_{\text{min}}$ ) and the detector ( $B_D$ ). The maximum acceptance angle is then

$$\theta_{\text{max}} = \arcsin \sqrt{\frac{B_S}{B_{\text{max}}}} \approx 50.5^\circ. \quad (2.3)$$

With this configuration, the energy resolution of the MAC-E filter is defined by

$$\Delta E = E \cdot \frac{B_{\text{min}}}{B_S} \cdot \frac{\gamma + 1}{\gamma_{\text{ana}} + 1} \cdot \sin^2(\theta_{\text{max}}) = E \cdot \frac{B_{\text{min}}}{B_{\text{max}}} \cdot \frac{\gamma + 1}{\gamma_{\text{ana}} + 1} \quad (2.4)$$

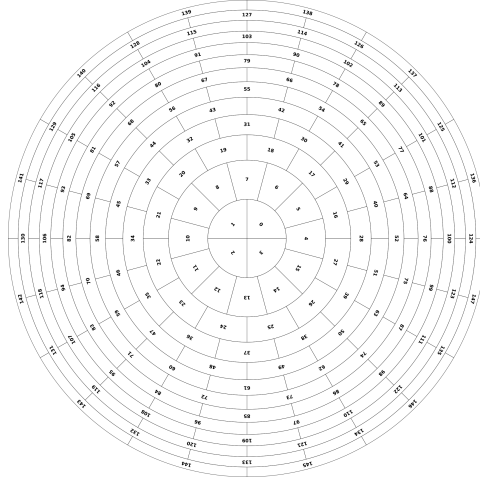


Figure 2.3: Schematic view of the KATRIN 148-pixel focal plane detector (FPD) with its dart-board arrangement.

with the relativistic gamma factor in the analyzing plane  $\gamma_{\text{ana}}$  (see [34] for more details). This means the KATRIN experiment reaches an energy resolution of  $\Delta E = \mathcal{O}(1 \text{ eV})$ .

### 2.1.5 Detector section

The focal plane detector (FPD) of the KATRIN experiment is a silicon *p-i-n*-diode array with 148 pixels. Electrons that pass the MS are accelerated by a post acceleration electrode (PAE) at a typical voltage of 10 kV and are measured by the detector. The PAE shifts the signal energy peak into a region of lower intrinsic background (see [39] for more details) and reduces the backscattering probability of the electrons. The dart-board arrangement of the  $44 \text{ mm}^2$  pixels (see figure 2.3) allows for consideration and investigation of radial and azimuthal effects. The mean energy resolution of all pixels is 1.85 keV full width half maximum (FWHM) for 59.54 keV [28] which allows a region-of-interest (ROI) cut on the detected energy to further decrease the detector background. For the neutrino mass analysis, typically, not all pixels are used (see section 4.1.2 for more details).

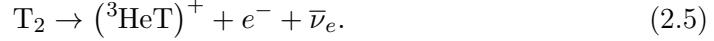
## 2.2 Modelling of the $\beta$ -decay spectrum

In the following, the model of the  $\beta$ -decay spectrum, which describes the expected count rate measured with the KATRIN experiment, is derived. It combines effects

altering the differential decay spectrum from equation 1.10 with the response function of the experimental setup.

### 2.2.1 Final states distribution

The differential rate described with equation 1.10 and shown in figure 1.2 is valid for the  $\beta$ -decay of atomic tritium. However, in the KATRIN experiment, a molecular tritium source is used (see section 2.1.2):



The daughter molecule  $({}^3\text{HeT})^+$  may end up in a rotational, vibrational or electronic excited state  $f$  with the probability  $P_f$ . This needs an extra amount of energy  $V_f$ , which is described by the final states distribution (FSD). It can be calculated theoretically (see [40] for more details) and is shown in figure 2.4. The FSD influences the differential  $\beta$ -decay rate in the following way:

$$\begin{aligned} \frac{d\Gamma}{dE}(E) = & \frac{G_F^2 \cos^2(\theta_C)}{2\pi^3} \cdot |M_{\text{nuc}}|^2 \cdot F(Z', E) \cdot p \\ & \cdot (E + m_e) \cdot \sum_f P_f \cdot \epsilon_f \cdot \sqrt{\epsilon_f^2 - m_\beta^2} \cdot \Theta(\epsilon_f - m_\beta) \end{aligned} \quad (2.6)$$

with the reduced neutrino energy  $\epsilon_f = E_0 - E - V_f$ .

### 2.2.2 Doppler effect

The gas molecules of the gaseous tritium source are constantly in thermal motion. This leads to an additional Doppler broadening of the  $\beta$ -decay spectrum [31]:

$$\sigma_D = \sqrt{2Ek_B T \cdot \frac{m_e}{m_{\text{T}_2}}} \quad (2.7)$$

with the Boltzmann constant  $k_B$ , the temperature of the source  $T$  and the mass ratio of an electron and a tritium molecule  $\frac{m_e}{m_{\text{T}_2}}$ . For the typical KATRIN neutrino mass measurement configuration ( $E = E_0 \approx 18.6$  keV,  $T \approx 80$  K) the Doppler broadening has a value of  $\sigma_D \approx 150$  meV. It changes the differential spectrum from equation 2.6 to

$$\frac{d\Gamma}{dE}(E) \rightarrow \int_{-\infty}^{+\infty} g(E - \epsilon) \frac{d\Gamma}{dE}(\epsilon) d\epsilon \quad (2.8)$$

with the normal distribution

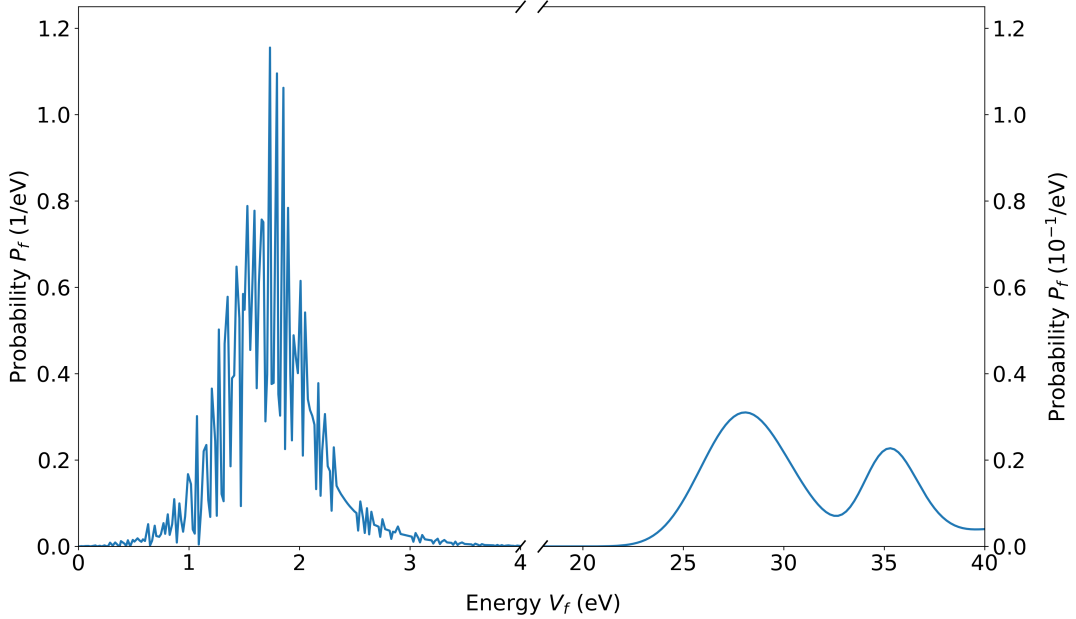


Figure 2.4: Final states distribution of molecular tritium  $T_2$  calculated for a temperature of 30 K. After the  $\beta$ -decay of  $T_2$ , the daughter molecule  $({}^3\text{HeT})^+$  may end up in a rotational, vibrational or electronic excited state with a certain energy  $V_f$  and probability  $P_f$ . The part below 4 eV describes transitions into the electronic ground state of  $({}^3\text{HeT})^+$ . The higher energies describe electronically excited states and the dissociation continuum. Adapted from [25].

$$g(E - \epsilon) = \frac{1}{\sqrt{2\pi}\sigma_D} \cdot \exp\left(-\frac{(E - \epsilon)^2}{2\sigma_D^2}\right). \quad (2.9)$$

In practice, additional broadenings (not limited to  $\sigma_D$ ) are emulated in the final states distribution (see [34] for more details).

### 2.2.3 Experimental response function

The response function  $R(E; qU)$  of the KATRIN experiment describes the probability of an  $\beta$ -electron with energy  $E$  to overcome the retarding potential  $qU$  of the MS and get counted by the focal plane detector. Ideally,  $R(E; qU)$  would be a simple step function (see figure 2.5):

$$R(E; qU) = \begin{cases} 1 & E \geq qU \\ 0 & E < qU \end{cases}. \quad (2.10)$$

This ideal response function gets altered by two dominating effects regarding the experimental setup, which will be explained in more detail in this chapter: The transmission properties of the MAC-E filter and scattering effects in the source.

### Transmission properties of the MAC-E filter

As described in section 2.1.4, the retarding potential  $qU$  of the analyzing plane in the MS is only sensitive to the longitudinal component of the electrons' energy  $E_{\parallel}$ . This leads to a finite energy resolution  $\Delta E$  of the spectrometer (equation 2.4), defined by the residual transversal electron energy  $E_{\perp}$  in the analyzing plane. This means that not all electrons with higher total energy  $E$  than the retarding energy  $qU$  can surpass the MAC-E filter and are measured.

For a given  $E$ , only electrons with a starting angle  $\theta$  which fulfills

$$\cos(\theta) > \sqrt{1 - \frac{E - qU}{E} \cdot \frac{B_S}{B_{\min}} \cdot \frac{\gamma_{\text{ana}} + 1}{\gamma + 1}} \quad (2.11)$$

can overcome  $qU$  (see [34] for the full derivation).

Equation 2.11 shows that electrons with  $E < qU$  can never pass the retarding potential, and those with  $E \geq qU + \Delta E$  always pass it.

This leads to the transmission function of the spectrometer

$$T(E; qU) = \begin{cases} 0 & E < qU \\ 1 - \sqrt{1 - \frac{E - qU}{E} \cdot \frac{B_S}{B_{\min}} \cdot \frac{\gamma_{\text{ana}} + 1}{\gamma + 1}} & qU \leq E < qU + \Delta E \\ 1 - \sqrt{1 - \frac{B_S}{B_{\max}}} & E \geq qU + \Delta E \end{cases} \quad (2.12)$$

which is shown in figure 2.5<sup>3</sup>.

While travelling from the WGTS to the MS via the TPS, the  $\beta$ -electrons lose energy due to synchrotron radiation. This synchrotron loss must be included in the transmission function, which is explained in more detail in [34].

### Scattering effects

Before the  $\beta$ -electrons leave the WGTS, they can scatter inelastically on residual tritium gas and lose energy. To describe this effect precisely, two components are needed: The probability  $P_s$  of an electron to scatter  $s$  times and the amount of

<sup>3</sup>The representation of the transmission function of equation 2.12 still includes the fact that not all electrons can make it through the MS ( $T(qU; E) < 1$ ). In figure 2.5, the solid angle is treated independently of the transmission function (see equation 3.31 of [34]).

energy  $\epsilon$  the electron loses during this process. Latter is described by the energy loss function  $f_s(\epsilon)$ .

The probability  $P_s$  of an electron to scatter  $s$  times depends on its starting position in the source tube  $z$  ( $z \in [0, 1]$ ), its starting angle  $\theta$  and the amount of tritium gas it has to get through before leaving the source [34, 41]. This amount of gas is described by the column density  $\rho d$ , which is the gas density integrated over the source length.

$P_s$  is described by a Poissonian distribution

$$P_s(z, \theta; \rho d) = \frac{\mu(z, \theta; \rho d)^s}{s!} \cdot \exp(-\mu(z, \theta; \rho d)) \quad (2.13)$$

with the expected number of scatterings  $\mu(z, \theta; \rho d) = \frac{z \cdot \rho d}{\cos(\theta)} \cdot \sigma_{\text{inel}}$  and the energy-dependent inelastic scattering cross section  $\sigma_{\text{inel}}$  (see [42, 43] for more details).

Assuming isotropic emission, the average scattering probabilities  $\overline{P}_s$  are

$$\overline{P}_s = \frac{1}{1 - \cos(\theta_{\text{max}})} \int_0^{\theta_{\text{max}}} \sin(\theta) \int_0^1 P_s(z, \theta; \rho d) dz d\theta. \quad (2.14)$$

The parameterization of the energy loss function  $f_1(\epsilon)$  for one scattering was developed in [44]. It uses three Gaussians in the region between about 11 and 15 eV. The ionization continuum beyond this energy region is described by the relativistic binary-encounter-dipole (BED) model [45]:

$$f_1(\epsilon) = \begin{cases} \sum_{i=1}^3 a_i \exp\left(-\frac{(\epsilon - m_i)^2}{2\sigma_i^2}\right) & \epsilon \leq E_i \\ \frac{f(E_i)}{f_{\text{BED}}(E_i)} \cdot f_{\text{BED}}(\epsilon) & \epsilon > E_i \end{cases} \quad (2.15)$$

with the amplitudes  $a_i$ , means  $m_i$  and widths  $\sigma_i$  ( $i = 1, 2, 3$ ) of the three Gaussians, respectively, the functional form of the BED model  $f_{\text{BED}}(\epsilon)$  and the ionization threshold  $E_i = 15.486$  eV for  $T_2$  [41].

For higher order scatterings  $s > 1$ , the energy loss function for one scattering  $f_1(\epsilon)$  (equation 2.15) has to be convolved  $(s-1)$ -times with itself. The energy loss function for zero scatterings is a Dirac delta function  $f_0(\epsilon) = \delta(\epsilon)$ .

Combining these scattering effects with the earlier described transmission properties of the MAC-E filter (see equation 2.12), the response function  $R(E; qU)$  of the KATRIN experiment is

$$R(E; qU) = \int_0^{E-qU} \sum_{s=0}^{\infty} \overline{P}_s \cdot T(E - \epsilon; qU) \cdot f_s(\epsilon) d\epsilon. \quad (2.16)$$

which is shown in figure 2.5.

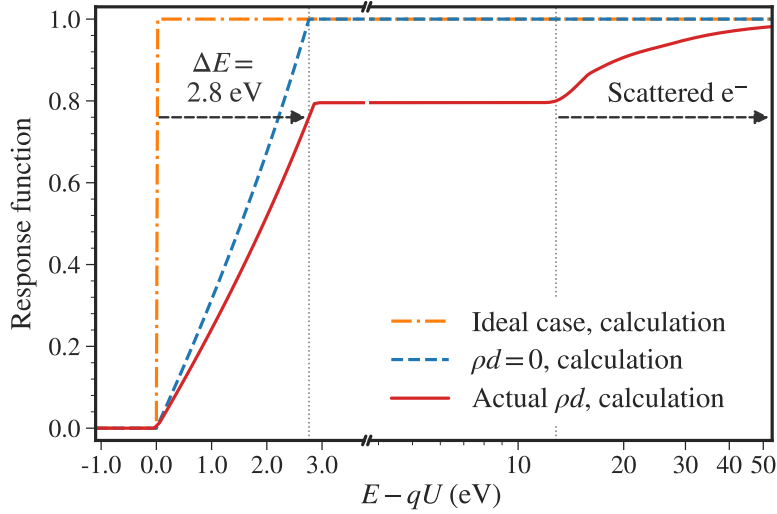


Figure 2.5: Response function  $R(E; qU)$  of the KATRIN experimental setup. It describes the probability of an  $\beta$ -electron with energy  $E$  to overcome the retarding potential  $qU$  of the MS. In the ideal case, with infinitesimal filter width and no scattering effects, it is a simple step function (orange dash-dotted line). Including the transmission properties of the MAC-E filter (without scattering effects, i.e. column density  $\rho d = 0$ ), the response function is broadened by the spectrometer's finite energy resolution  $\Delta E$  (blue dashed line). The combination of the transmission properties with scattering effects in the source leads to the actual experimental response function (red line). At higher surplus energies also electrons which scattered on residual tritium molecules and lost some energy, can overcome the retarding potential. Taken from [32].

#### 2.2.4 Model of the expected rate

To complete the model of the integral  $\beta$ -decay spectrum describing the expected count rate  $r(qU)$  measured at the retarding potential  $qU$ , the differential  $\beta$ -decay spectrum  $\frac{d\Gamma}{dE}(E)$  (see section 2.2.1 and 2.2.2) is integrated over the experimental response function  $R(E; qU)$  from equation 2.16

$$r(qU) = A \cdot \int_{-\infty}^{+\infty} \frac{d\Gamma}{dE}(E) \cdot R(E; qU) dE + B \quad (2.17)$$

and the normalization factor  $A = N_{\text{eff}} \cdot \frac{1 - \cos(\theta_{\text{max}})}{2} \cdot \epsilon_{\text{detector}}$  with the effective number of tritium atoms  $N_{\text{eff}}$  and the detector efficiency  $\epsilon_{\text{detector}}$ , and a constant background rate  $B$  are introduced.

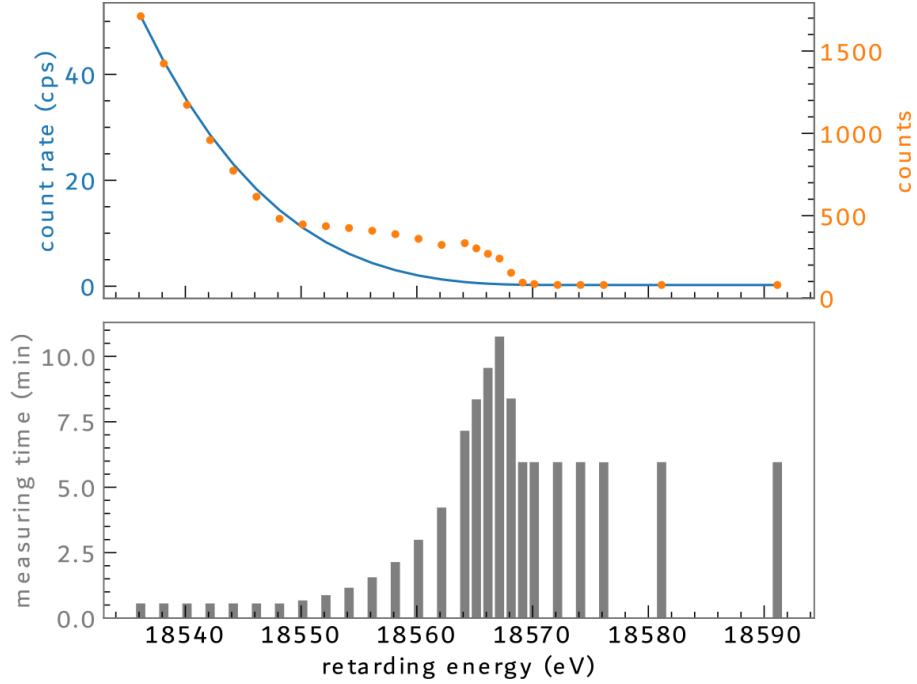


Figure 2.6: Example of a measuring time distribution (MTD) for KATRIN neutrino mass measurements. It defines the time  $t_i$  spent at each retarding voltage set point  $qU_i$ . The MTD at the bottom, together with the expected integral  $\beta$ -decay rate  $r(qU)$  from equation 2.17 (blue) at the top, leads to the expected number of counts (orange). Taken from [34].

A so-called KATRIN neutrino mass (KNM) campaign consists of a few hundred so-called  $\beta$ -scans or runs. Each  $\beta$ -scan involves sweeping the retarding voltage  $U$  across a fixed set of up to 40 points [25]. These voltage set points  $U_i$  reach from  $U_{\min} \sim 18\,300\text{ V}$  ( $qU_{\min} \sim E_0 - 300\text{ eV}$ ) to  $U_{\max} \sim 18\,735\text{ V}$  ( $qU_{\max} \sim E_0 + 135\text{ eV}$ ). It should be mentioned that for the neutrino mass analysis, only the data points above  $E_0 - 40\text{ eV}$  (the so-called 40 eV analysis range) are used [25]. At each  $qU_i$ , the time  $t_i$  is spent, typically between 30 and 1300 s. This means the model  $\mu_i$  describing the expected number of counts is

$$\mu_i = \mu_i(qU_i, t_i) = r(qU_i) \cdot t_i. \quad (2.18)$$

The so-called measurement time distribution (MTD), shown in figure 2.6, defines how much time  $t_i$  is spent at each retarding energy set point  $qU_i$ . The MTD used for the KATRIN neutrino mass measurements is optimized for maximal neutrino mass sensitivity [46].

## 2.3 Systematic uncertainties

For the KATRIN analysis, a precise description of the shape of the  $\beta$ -decay spectrum and all relevant systematic effects with their uncertainties is crucial. In general, systematic uncertainties emerge from the finite precision, with which model parameters can be determined and from instabilities of experimental parameters. In the following, all systematic effects of the KATRIN experiment are introduced and explained (see [32] for more details).

### 2.3.1 Source-related uncertainties

The systematic effects connected to the WGTS originate from scattering effects (compare section 2.2), from the plasma generated in the source tube and from the RW<sup>4</sup>.

#### Column density

As described in section 2.2, in the WGTS, the  $\beta$ -electrons scatter  $s$ -times on residual tritium molecules with a certain probability  $P_s$  (equation 2.13). This probability depends on  $\rho d\sigma_{\text{inel}}$ , the column density times the energy-dependent inelastic scattering cross section  $\sigma_{\text{inel}}$ . To obtain the mean value of  $\rho d\sigma_{\text{inel}}$ , that is present during a measurement campaign, two different calibration methods are used [25, 32].

The first one utilizes the e-gun in the RS, which emits electrons at a constant rate with well-defined energy and angle. These electrons travel through the entire source and undergo scatterings. By tuning the retarding potential  $qU$  of the MS while keeping the e-gun energy  $E$  constant, the shape of the experimental response function  $R(E; qU)$  from equation 2.16 (see figure 2.5) can be scanned. The value for  $\rho d\sigma_{\text{inel}}$  is obtained by a fit to the measured response function. Several of these e-gun measurements are performed during one measurement campaign, usually one per week.

The second calibration method uses dedicated pressure sensors, flow meters and the tritium rate, which scales with  $\rho d$ , to monitor short-term variations of the column density.

Combining both calibration methods allows an accurate determination of  $\rho d\sigma_{\text{inel}}$  for each measurement campaign. The total uncertainty on  $\rho d\sigma_{\text{inel}}$  arises from three contributions:

- The limited precision of the e-gun measurements regarding the e-gun angle and the e-gun background.

---

<sup>4</sup>In chapter 2.1, the RW was introduced as part of the RS. Because it controls the source potential, it can also be listed as part of the WGTS.

- The accuracy with which the short-term column density variations can be measured. This depends, for example, on the reproducibility of the flow meter.
- The scaling of  $\sigma_{\text{inel}}$  to a lower electron energy. The e-gun measurements are performed with a higher electron energy than the tritium endpoint energy of  $E_0 \approx 18.6$  keV.

## Energy loss function

In addition to the scattering probability  $P_s$  also, the energy loss function  $f_s(\epsilon)$  (compare equation 2.15), which describes the amount of energy the electron loses during  $s$ -times scatterings, is substantial for the description of scattering effects in the gaseous source. All parameters describing the energy loss function are determined by two dedicated e-gun measurement methods, the so-called integral and differential measurements (see [41, 44] for more details). The former approach is a fine-binned measurement of the response function  $R(E; qU)$  from equation 2.16 by changing the energy  $E$  of the monoenergetic e-gun electrons while keeping the retarding potential  $qU$  constant. The differential measurement method uses time-of-flight information from e-gun measurements with a pulsed laser source, which allows to directly measure the electron energy spectrum. The values, uncertainties and correlations of the energy loss parameters are obtained from fits to the described measurements.

## Source plasma

As described in section 2.1.4, the retarding voltage  $U$  is applied to the MS to reflect all  $\beta$ -electrons with a lower energy than  $qU$  (with  $q = e$ ). In addition to the absolute value of  $qU$ , the starting potential of the electrons has to be considered. This starting potential is provided by the strongly magnetized cold plasma in the WGTS [28]. This plasma occurs due to the emitted  $\beta$ -electrons, the ionized daughter nuclei ( ${}^3\text{HeT}^+$ ) of the decays and secondary electrons produced via scatterings [47]. Ideally, the source plasma would have a homogeneous distribution. In reality, this is not the case. There are spatial, i.e. radial, azimuthal and longitudinal, and time-dependent inhomogeneities present, which have to be considered during the analysis.

The radial and azimuthal plasma inhomogeneities can be included in the model via the segmentation of the detector in its individual pixels. The pixel-wise starting potentials lead to pixel-wise retarding energies  $qU_{\text{px}}$  which can be absorbed by pixel-wise endpoints  $E_{0,\text{px}}$  [34].

However, this is not applicable for longitudinal inhomogeneities [47]. Two parameters are introduced to account for these in the model: A potential broadening with variance  $\sigma_z^2$  and a shift  $\epsilon_z$  of the energy loss function. Latter comes from the fact that  $\beta$ -electrons, which are emitted further away from the detector, have a higher probability of undergoing scatterings because they must travel further through the

gaseous source. If the source potential has a longitudinal gradient, electrons which scatter a certain number of times start at another average source potential than those which scatter less or more often.

The value of the potential broadening  $\sigma_z$  can be determined via calibration measurements using  $^{83m}\text{Kr}$  [47]. With this value, an upper limit for the shift of the energy loss function  $\epsilon_z$  can be set:

$$|\epsilon_z| < \frac{\sigma_z}{\kappa} \quad (2.19)$$

with the parameter  $\kappa$  introduced in [47].

There are two types of time-dependent inhomogeneities. Short-term fluctuations of the plasma potential and potential drifts over more extended time periods. Both are included in the model via an additional broadening, respectively:  $\sigma_{\text{short-term}}$  and  $\sigma_{\text{long-term}}$ .

The total broadening  $\sigma_{\text{plasma}}$  caused by the plasma potential is then

$$\sigma_{\text{plasma}}^2 = \sigma_z^2 + \sigma_{\text{short-term}}^2 + \sigma_{\text{long-term}}^2 \quad (2.20)$$

which can be included in the model as described in section 2.2.2.

## Rear wall

The RW was introduced in section 2.1.1. It is located at the upstream end of the WGTS (see section 2.1.2). Residual tritium molecules  $\text{T}_2$  from the source can hit the RW and accumulate there. The decays of these molecules lead to an underlying background tritium spectrum, which has to be added to the  $\beta$ -spectrum from the signal electrons. Three additional parameters are used to describe this RW spectrum: The rear wall endpoint  $E_{0,\text{RW}}$ , the rear wall FSD shape (compare section 2.2.1), and the rear wall activity [25]. The values of these parameters and their uncertainties are inferred from calibration measurements where the WGTS is empty, i.e. no tritium is circulated. The RW is regularly cleaned with ozone to decrease the impact of its background spectrum on the neutrino mass analysis [48].

## Activity fluctuations

Source activity fluctuations impact the normalization factor  $A$  of the expected integral  $\beta$ -decay rate  $r$  from equation 2.17. To account for this, the relative activity  $A_i$  at each retarding voltage set point would have to be measured and included in the model. Due to the limited accuracy of the  $A_i$  determination, an artificial bias could be introduced [34]. Instead, this systematic effect is neglected, given the small impact on the total neutrino mass uncertainty of  $< 0.001 \text{ eV}^2$  [25].

### 2.3.2 Background-related uncertainties

The dominant background component of the KATRIN experiment arises due to highly excited Rydberg atoms.  $^{210}\text{Po}$  is deposited in the spectrometer walls through the decay chain of  $^{222}\text{Rn}$ . Via the  $\alpha$ -decay of  $^{210}\text{Po}$ ,  $^{206}\text{Pb}$  is created, and atoms from the spectrometer surface are sputtered off due to the high nuclear recoil of the decay process. Black-body radiation can ionize these Rydberg atoms and create low-energy electrons inside the spectrometer. If this happens downstream w.r.t. the analyzing plane, the electrons are accelerated towards the FPD by the retarding potential and lead to a nearly constant, Poissonian background which scales with the volume between the analyzing plane and the detector [32, 49].

In the following, additional background components that deviate from the explained constant and Poissonian ones are described.

#### Background energy slope

The background rate shows a linear dependence of the retarding voltage  $qU$  [49, 50], which has to be added to the model. The constant background rate  $B$  introduced in equation 2.17 is expanded to

$$B(qU) = B + m_B \cdot (qU - 18575 \text{ eV}) \quad (2.21)$$

with the background slope  $m_B = \mathcal{O}(10^{-6} \text{ cps/eV})$ . The value of  $m_B$  can be measured with an empty WGTS.

#### Penning background

As mentioned in chapter 2.1.4, the combination of the PS and MS, both operating at high voltages, leads to the formation of a Penning trap (see [49, 51–53] for more details). Trapped electrons can ionize residual gas and generate ions and additional electrons. The ions can escape and reach the MS, where they create additional background electrons. This additional background component scales with the number of stored electrons in the Penning trap, i.e. with the time  $t$ . The Penning background is emulated by a quadratic function in the  $\beta$ -decay model [25].

Since the PS is not longer operated at high voltages, the Penning background is only present for the first four KATRIN measurement campaigns [25].

#### Background overdispersion

The last major background component of the KATRIN experiment is caused by high-energy electrons stored in the MS [49, 54]. The main source of these electrons is the decay of radon isotopes. If electrons created in the MS have a high enough transversal energy, they get trapped inside the spectrometer due to the magnetic

field configuration introduced in section 2.1.4. Since the escape is only possible if the electrons lose enough energy through scatterings or non-adiabatic motion, they are stored in the MS for several hours. During this time, the electrons create secondary electrons via ionization of residual gas. The secondary electrons are usually not stored and reach the detector if generated downstream w.r.t. the analyzing plane. Since these events are time-correlated, this additional background component is not Poissonian and leads to an overdispersion compared to the expected Poisson variance [34]. This is included in the model via a Gaussian widening, which leads to an increased statistical uncertainty.

The background overdispersion is not observed during measurement campaigns in the so-called shifted analyzing plane (SAP) setting (see section 2.3.3) since there the background electron storage condition is altered (see [55] for more details).

### 2.3.3 Electromagnetic-fields-related uncertainties

The MAC-E filter with its magnetic fields  $B_{\max}$ ,  $B_{\min}$  and  $B_S$  and the retarding potential  $qU$  in the analyzing plane introduced in section 2.1.4 is one of the main components of the KATRIN experiment. In the following, the influence of the uncertainties of these  $B$ -fields and the potential in the analyzing plane is described.

#### Magnetic fields

The transmission function  $T(E; qU)$  of the KATRIN MAC-E filter from equation 2.12 directly depends on the three magnetic fields  $B_{\max}$ ,  $B_{\min}$  and  $B_S$ . This has to be considered when propagating their uncertainties.

Also, the maximum acceptance angle  $\theta_{\max}$  (equation 2.3) is defined by  $B_S$  and  $B_{\max}$ , which influences the overall signal amplitude. Since the normalization factor  $A$  of the  $\beta$ -decay model from equation 2.17 is a free parameter (see section 2.4.1), this does not affect the neutrino mass analysis. However, for the scattering probabilities  $\overline{P_S}$  (equation 2.13), the angular change has to be considered since the upper integration limit changes. This effect influences the shape of the experimental response function from equation 2.16 [34].

#### Analyzing plane

As described in section 2.3.2, the background rate of the KATRIN experiment scales with the volume between the analyzing plane and the FPD. To decrease this volume and hence the background rate, the analyzing plane of the spectrometer was shifted towards the detector [55]. This led, on the one hand side, to a background reduction by a factor of  $\sim 2$  comparing the old so-called nominal analyzing plane (NAP) setting with the new so-called shifted analyzing plane (SAP) setting. However, on the other hand, the radial inhomogeneities of the magnetic field in the analyzing plane  $B_{\min}$

and the retarding potential  $qU$  increased. To take these into account, the pixels of the FPD with similar field values are grouped into patches for the neutrino mass analysis. This will be explained in more detail in section 4.1.2. Each patch is described by its own response function.

Due to the strong gradients of  $B_{\min}$  and  $qU$ , an additional broadening  $\sigma_{\text{ana}}$  of the transmission function has to be introduced. This broadening can be treated equivalently to the plasma broadenings described in section 2.3.1. Their variances are added (compare equation 2.20).

It should be noted that the two different analyzing plane settings were tested and compared during the third measurement campaign, which was afterwards split into two separate campaigns, KNM3-SAP and KNM3-NAP for the neutrino mass analysis. Since KNM4 only the SAP setting is used [25].

### 2.3.4 Detector-related uncertainties

Different physics and detector-related effects influence the detector efficiency. But because of the free normalization factor  $A$  in the  $\beta$ -decay model from equation 2.17 (see section 2.4.1), any effects independent of the retarding voltage  $U$  will not affect the spectral shape [32]. In the following, the four known  $U$ -dependent effects are explained (see [25] for more details). The uncertainties and biases related to these effects are too small to consider for the neutrino analysis [25, 34].

#### ROI-coverage

An electron is counted by the FPD if its energy falls into a predefined region of interest (ROI). The FPD energy spectrum changes with the retarding voltage set point  $U$ , but the ROI is fixed for all  $U$ . This leads to a  $U$ -dependent detector efficiency  $\epsilon_{\text{detector}}(qU)$ , which is modelled by a linear slope [34].

#### Pile-up

Pile-up happens when multiple electrons hit the FPD simultaneously and cannot be distinguished as separate events. Rather than detecting two events with energies  $E_1$  and  $E_2$ , a single event with combined energy  $E_1 + E_2$  is registered. If  $E_1 + E_2$  exceeds the ROI, neither electron is counted as an individual event. The probability of pile-up events is influenced by the overall electron rate, which depends on the retarding potential  $qU$ . This is also included in the model as a  $U$ -dependent detector efficiency [25].

## Back scattering

If an electron is reflected by the FPD and not reflected back by the post acceleration introduced in section 2.1.5 or the spectrometer fields, it is lost to the source. The probability for backscattering events depends on the retarding voltage set point  $U$  because the escape to the source is more likely for lower retarding energies  $qU$ . Since the backscattering probability varies with the incident angle and the repeated traversal through the detector dead layer alters the measured spectral shape, a slight angular dependence is present. This effect is considered as a modification of the transmission function [25].

## Gain and resolution fluctuations

The gain and resolution of the FPD can drift over time. This effectively leads to a detection efficiency dependent on the retarding voltage set point  $U$ . This effect is not included in the model since the bias on the neutrino mass squared  $m_\nu^2$  was found to be less than  $10^{-4} \text{ eV}^2$  [25].

### 2.3.5 FSD-related uncertainties

The FSD and its impact on the  $\beta$ -decay model were introduced in section 2.2.1. There are different types of uncertainties of the FSD obtained from theoretical calculations, four with origin in the theory and calculation itself, and one with experimental origin (see [40] for more details):

- Uncertainties due to the adapted approximations
- Uncertainties in constants of the calculations
- Uncertainties due to finite numerical precision
- Possibility of wrong computer code and input files
- Uncertainty of the measured source temperature and the isotopologue composition, which leads to a sum of FSDs

Since the contribution of the total FSD uncertainty to the total neutrino mass uncertainty is  $< 0.001 \text{ eV}^2$ , it is not propagated by the fit [25].

## 2.4 Analysis strategies

The KATRIN experiment aims to measure the effective electron anti-neutrino mass  $m_\nu$  (equation 1.11). In the following, the strategies to infer a value and uncertainty for  $m_\nu$  are described.

### 2.4.1 Maximum likelihood method

The likelihood function  $\mathcal{L}(\mu(\vec{\theta}); x)$  describes the probability to measure a specific outcome  $x$  of an experiment under the assumption of the model  $\mu = \mu(\vec{\theta})$ , which depends on the set of parameters  $\vec{\theta}$  [56]. To determine the values of  $\vec{\theta}$  with which the model  $\mu(\vec{\theta})$  best describes the data  $x$ , the likelihood function is maximized with respect to  $\vec{\theta}$ . It should be noted that in practice, it is favourable to minimize  $-\ln(\mathcal{L})$  instead of maximizing  $\mathcal{L}$  due to numerical stability [34].

As described in section 2.2.4, the KATRIN experiment measures the number of counts  $N_i$  at a retarding potential set point  $qU_i$  for the time  $t_i$ . The model  $\mu_i$ , which predicts this number of counts, is defined in equation 2.18. Since the individual  $\beta$ -decays are statistically independent of each other, the probability  $P(N_i; \mu_i)$  to measure  $N_i$  counts is described by the probability mass function (PMF)

$$P(N_i; \mu_i) = \frac{\mu_i^{N_i}}{N_i!} \cdot e^{-\mu_i}, \quad (2.22)$$

which is the Poisson distribution.

The total measured integral  $\beta$ -decay spectrum consists of a set of retarding potentials  $\vec{qU}$  with the associated measurement times  $\vec{t}$ , which is described by the MTD (see figure 2.6). The individual measurements are statistically independent of each other, i.e. the joint PMF for all measured counts  $\vec{N}$  and model predictions  $\vec{\mu}$  is the product of the individual PMFs from equation 2.22:

$$P(\vec{N}; \vec{\mu}) = \prod_i P(N_i; \mu_i) = \prod_i \frac{\mu_i^{N_i}}{N_i!} \cdot e^{-\mu_i}. \quad (2.23)$$

At the same time, this joint PMF is the general KATRIN likelihood

$$\mathcal{L}(\vec{\theta}; \vec{N}, \vec{qU}, \vec{t}) = \prod_i P(N_i; \mu_i(\vec{\theta}, qU_i, t_i)). \quad (2.24)$$

In addition to the effective neutrino mass squared  $m_\nu^2$ , the endpoint energy  $E_0$ , the normalization factor  $A$  and the constant background rate  $B$  build the set of free parameters  $\vec{\theta}_{\text{free}} = \{m_\nu^2, E_0, A, B\}$ , which are inferred directly from the data (compare equation 2.17). The model for the likelihood analysis is then

$$\mu_i(m_\nu^2, E_0, A, B, qU_i, t_i) = \left( A \cdot \int_{qU}^{E_0} \frac{d\Gamma}{dE}(E; m_\nu^2, E_0) \cdot R(E; qU_i) dE + B \right) \cdot t_i. \quad (2.25)$$

For a large number of counts  $N_i$  the Poisson distributions of equation 2.23 converge to normal distributions with mean  $\mu_i$  and standard deviation  $\sqrt{\mu_i} \approx \sqrt{N_i}$  [56]:

$$P(\vec{N}; \vec{\mu}) = \prod_i \frac{1}{\sqrt{2\pi N_i}} \cdot e^{-\frac{(N_i - \mu_i)^2}{2N_i}}. \quad (2.26)$$

In this case minimizing  $-\ln(\mathcal{L})$  is equivalent to the  $\chi^2$ -minimization:

$$-\ln(\mathcal{L}(\vec{\mu}; \vec{N})) \propto \sum_i \frac{(N_i - \mu_i)^2}{2N_i} =: \frac{1}{2}\chi^2(\vec{\mu}; \vec{N}). \quad (2.27)$$

Now, knowing the values of  $\vec{\theta}$  with which the model  $\mu(\vec{\theta})$  best describes the data, the confidence interval of a given parameter  $\theta$ , e.g.  $m_\nu^2$  can be determined. It describes which other values of  $m_\nu^2$  are generally compatible with the data (see [34] for more details). For that, the profile likelihood is used. It utilizes Wilk's theorem [57] with the test statistic

$$-2 \log \left( \frac{\mathcal{L}(H_0)}{\mathcal{L}(H_1)} \right) = 2 \cdot (\log(\mathcal{L}(H_1)) - \log(\mathcal{L}(H_0))) =: 2\Delta \log(\mathcal{L}) \geq 0. \quad (2.28)$$

Here,  $H_0$  is the null hypothesis with the parameter values that best describe the data, and  $H_1$  is the alternative hypothesis with another set of values, in this example, a different value for  $m_\nu^2$ , which is tested to see if it falls into the confidence interval.

Using the  $1\sigma$  confidence interval as an example, this means the values of  $m_\nu^2$ , for which  $2\Delta \log(\mathcal{L}) = 1$ , have to be determined. These values then build the confidence interval.

### 2.4.2 Data combination

When analyzing the KATRIN data, its segmentation must be considered. On the one side, the FPD has 148 different pixels (see section 2.1.5), which, in general, all measure their own integral  $\beta$ -spectrum. On the other side, the KATRIN data set consists of multiple  $\beta$ -scans measured in different KNM campaigns with eventually different settings as described in section 2.2.4. In the following, the combination of the KATRIN data is discussed, and the derivation of a single likelihood function describing this combined data is presented.

#### Pixel combination

All measured integral  $\beta$ -spectra by the individual pixels of the FPD are statistically independent of each other. This allows the extension of the likelihood function  $\mathcal{L}$  from equation 2.24 by another dimension:

$$\mathcal{L}(\vec{\theta}; \vec{N}, \vec{qU}, \vec{t}) = \prod_{\text{px}} \prod_i P(N_{\text{px},i}; \mu_{\text{px},i}(\vec{\theta}_{\text{px}}, qU_{\text{px},i}, t_i)) \quad (2.29)$$

where the outer product loops over all pixels  $px$  and the inner product over all retarding energy set points  $i$ . While there are shared parameters which are equal for every pixel, e.g. the neutrino mass squared  $m_\nu^2$ , there are also some which have individual values for every pixel, e.g. the magnetic field in the analyzing plane  $B_{\min}$  as described in section 2.3.3. This leads, in general, to pixel-wise sets of parameters  $\vec{\theta}_{px}$ . This approach is called multi-pixel combination [34].

On the one hand, the multi-pixel combination is the most general approach, but on the other side, it is also the most computationally expensive one since it has the most model evaluations possible. To reduce the dimensionality of the analysis and at the same time maintain the accuracy of the model, the segmentation of detector pixels with similar properties into patches, as described later in section 4.1.2, is introduced. Each patch receives a spectrum by summing the counts of the pixels belonging to that patch [34]. With this so-called multi-patch combination, the likelihood function is

$$\mathcal{L}(\vec{\theta}; \vec{N}, \vec{qU}, \vec{t}) = \prod_{\text{patch}} \prod_i P(N_{\text{patch},i}; \mu_{\text{patch},i}(\vec{\theta}_{\text{patch}}, qU_{\text{patch},i}, t_i)). \quad (2.30)$$

where the outer product now loops over all patches.

In the extreme case of defining only one patch, this is called uniform combination, the outer loop disappears and the likelihood function is again defined by equation 2.24. Now, the neglected radial dependencies of systematic parameters, e.g. of the source plasma (section 2.3.1) or the magnetic field in the analyzing plane (section 2.3.3) lead to a significant shift of the neutrino mass squared  $m_\nu^2$  (see table 1 of [31]). However, if the statistical uncertainty dominates over the systematic shift of  $m_\nu^2$ , the uniform combination approach is usable [58].

### $\beta$ -scan combination

As described in section 2.2.4, one KNM campaign consists of a few hundred  $\beta$ -scans. Each scan is an individual measurement of the integral  $\beta$ -spectrum, where the MTD defines how much time  $t_i$  is spent at each retarding potential set point  $qU_i$  (see figure 2.6). I.e. an extension of the likelihood function  $\mathcal{L}$  from equation 2.24 by another dimension, analogous to the pixel combination (equation 2.29), is possible:

$$\mathcal{L}(\vec{\theta}; \vec{N}, \vec{qU}, \vec{t}) = \prod_s \prod_i P(N_{s,i}; \mu_{s,i}(\vec{\theta}_s, qU_{s,i}, t_{s,i})) \quad (2.31)$$

where the outer product now loops over all individual  $\beta$ -scans  $s$  and the inner one again over all retarding set points  $i$ .

However, this combination approach is very computationally expensive due to the large number of data points. Since all slow control parameters are kept stable at or

below the percentage level throughout one measurement campaign and in addition, the reproducibility of the high voltage set points is excellent at the parts-per-million level [59–61], the so-called stacking of the data is possible [34]. There the counts and measurement times of all  $\beta$ -scans are summed up for every individual retarding voltage set point  $qU_i$ . After the summation, the average  $qU$  values of all  $\beta$ -scans are used, and the model parameters are averaged over the KNM campaign.

If the MTD changes during a measurement campaign, the simple stacking of the data is no longer possible. In that case, a more advanced clustering algorithm is used (see [34] for more details).

### KNM campaign combination

For the data combination of different KNM campaigns, the stacking approach used for  $\beta$ -scans within one campaign is unsuitable due to changing slow control parameters between the individual campaigns (see e.g. [25]). This leads to the following extension of the likelihood function  $\mathcal{L}$  from equation 2.24, analogous to the pixel combination (equation 2.29):

$$\mathcal{L}(\vec{\theta}; \vec{N}, \vec{qU}, \vec{t}) = \prod_c \prod_i P(N_{c,i}; \mu_{c,i}(\vec{\theta}_c, qU_{c,i}, t_{c,i})) \quad (2.32)$$

where the outer product now loops over all individual KNM campaigns  $c$  and the inner one over all stacked retarding set points  $i$  within the campaign.

### Combined likelihood function

The junction of all previously introduced combination approaches leads to the combined KATRIN likelihood function

$$\mathcal{L}(\vec{\theta}; \vec{N}, \vec{qU}, \vec{t}) = \prod_c \prod_{\text{patch}} \prod_i P(N_{c,\text{patch},i}; \mu_{c,\text{patch},i}(\vec{\theta}_{c,\text{patch}}, qU_{c,\text{patch},i}, t_{c,i})). \quad (2.33)$$

This takes into account varying model parameters  $\vec{\theta}$  for different measurement campaigns  $c$  and detector patches. The number of counts  $N$  is stacked for every voltage set point  $qU$  and every patch. The times  $t$  are stacked for every voltage set point  $qU$ .

#### 2.4.3 Treatment of systematic effects

Two different approaches can be used to include the systematic effects described in chapter 2.3 into the analysis. Each of them is explained in the following.

### Nuisance parameter method

During the so-called nuisance parameter or pull term method, the systematic parameters  $\vec{\theta}_{\text{syst}}$  are enabled for the likelihood maximization explained in section 2.4.1 in addition to the set of free model parameters  $\vec{\theta}_{\text{free}} = \{m_{\nu}^2, E_0, A, B\}$ , which was introduced in chapter 2.4.1. Furthermore, the parameters  $\vec{\theta}_{\text{syst}}$  are constrained by so-called pull terms  $f(\vec{\theta}_{\text{syst}})$ , which are included into the likelihood function  $\mathcal{L}$ :

$$\mathcal{L}(\vec{\theta}_{\text{free}}) \rightarrow \mathcal{L}(\vec{\theta}_{\text{free}}, \vec{\theta}_{\text{syst}}) \cdot f(\vec{\theta}_{\text{syst}}) \quad (2.34)$$

Typically, the pull terms are normal distributions for one systematic parameter  $\theta_{\text{syst}}$  with the best value  $\mu$  and the Gaussian uncertainty  $\sigma$ , which are determined, e.g. via calibration measurements:

$$f(\theta) \propto e^{-\frac{(\theta-\mu)^2}{2\sigma^2}}. \quad (2.35)$$

### Monte Carlo propagation

To propagate systematic effects into the fit via the Monte Carlo sampling method, there are four steps necessary:

1. Draw a value for one systematic parameter  $\theta_{\text{syst}}$  regarding to its probability density function (PDF).
2. Calculate the integral  $\beta$ -decay spectrum from equation 2.17 with the previously drawn value for  $\theta_{\text{syst}}$ .
3. Fit the calculated spectrum and retrieve the results for the free fit parameters  $\vec{\theta}_{\text{free}}$ .
4. Repeat this procedure very often to get the distributions of the free fit parameters.

The systematic uncertainties  $\vec{\sigma}_{\text{syst}}$  on  $\vec{\theta}_{\text{free}}$ , due to the systematic parameter  $\theta_{\text{syst}}$ , are reflected by the widths of the distributions.

To get the total uncertainty  $\sigma_{\text{tot}}$ , the described procedure is carried out while drawing values for all systematic parameters simultaneously in step 1 and, in addition to that, fluctuating the spectrum regarding a Poisson distribution (compare equation 2.22).

### 2.4.4 Software

For the work presented in this thesis, two existing analysis software packages were used: *Fitrium* [58] and *Netrium* [34, 62], both were developed by Dr. Christian Karl et al. and are briefly introduced in the following.

*Fitrium* (Fit Tritium) is written entirely in the C++ programming language. It includes a complete model of the  $\beta$ -decay of molecular tritium and applications for Monte Carlo data generation and data fitting.

For the fitting of data, the model from equation 2.17 has to be evaluated multiple times, e.g.  $\mathcal{O}(10^{10})$  for one measurement campaign with the segmentation of the FPD into 14 patches (compare section 2.4.2) using the nuisance parameter method described in section 2.4.3. This can take up to one CPU year [62]. To speed up the calculations by about three orders of magnitude and at the same time maintain the accuracy requirements for the KATRIN analysis, *Netrium* was developed. It uses a neural network to learn the predicted integral  $\beta$ -decay spectrum from equation 2.17 and its dependence on all relevant input parameters  $\vec{\theta}_{\text{spec}}$ .

The architecture of the *Netrium* neural network is shown in figure 2.7. Its inputs are the parameters  $\vec{\theta}_{\text{spec}}$  influencing the integral  $\beta$ -spectrum  $r(qU; \vec{\theta}_{\text{spec}})$  from equation 2.17. It should be noted that the normalization factor  $A$  and the background rate  $B$  are not included in the neural network. The count rate, predicted by the model at each  $qU$  point, corresponds to the outputs of the network. There are two fully connected hidden layers with 128 nodes each between the input and output layers.

For the training of the neural network,  $\mathcal{O}(10^6)$  input samples are used, which are generated by *Fitrium*. For this sample generation, the input parameters  $\vec{\theta}_{\text{spec}}$  are drawn from uniform (for  $m_\nu^2$  and  $E_0$ ) and normal distributions within their expected  $3\text{-}\sigma$  range. For the sampling, the  $N$ -dimensional  $R_2$  method is used [63]. The sample generation is embarrassingly parallel, which means the required computing time of  $\mathcal{O}(10^1)$  CPU years can be split upon thousands of CPUs on a computing cluster. This allows completing this task within a single day [62].

During the training, the weights of the neural network are optimized to minimize the loss function

$$\text{loss}(\text{weights}) = \langle (C_i - C_{\text{pred},i}(\text{weights}))^2 \rangle \quad (2.36)$$

with the true rate change  $C_i = \frac{r_i}{\langle r_i \rangle}$  of every sample and the corresponding prediction of the neural network  $C_{\text{pred},i}(\text{weights})$ . Since all tritium spectra have roughly the same shape, the rates  $r_i$  are divided by the sample mean  $\langle r_i \rangle$  at each  $qU_i$  point.

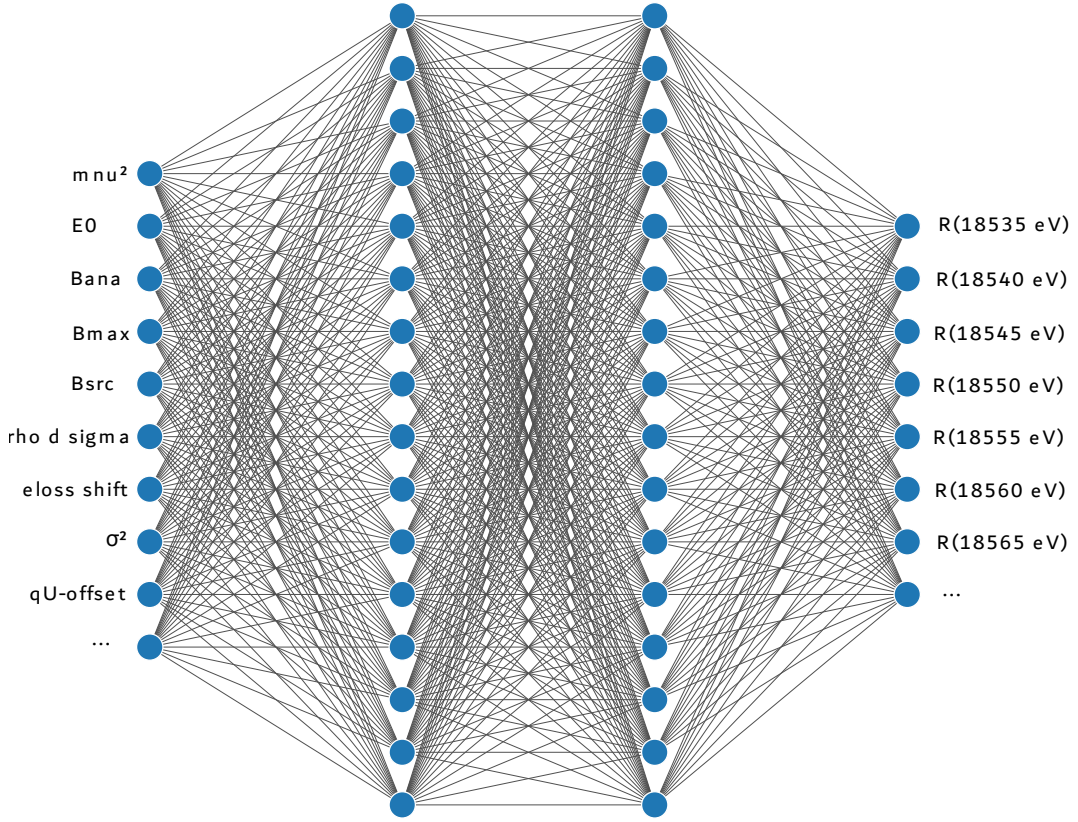


Figure 2.7: Sketch of the architecture of the *Netrium* neural network. Its inputs are the parameters  $\vec{\theta}_{\text{spec}}$  influencing the integral  $\beta$ -decay spectrum  $r(qU; \vec{\theta}_{\text{spec}})$  from equation 2.17. The count rate, predicted by the model at each  $qU$  point, corresponds to the outputs. There are two fully connected hidden layers with 128 nodes each between the input and output layers. Taken from [34].

## 2.5 Current KATRIN neutrino mass result

The current KATRIN neutrino mass result was published in June 2024 [25]. For this analysis, the data of the first five KNM campaigns was used, which corresponds to approximately 20% of the final statistics. The best fit result of the neutrino mass squared was  $m_\nu^2 = -0.14_{-0.15}^{+0.13} \text{eV}^2$ , which leads to an upper limit of  $m_\nu < 0.45 \text{eV}$  (90% C.L.). In figure 2.8, which shows the individual components of the total uncertainty  $\sigma_{\text{tot}}$  on  $m_\nu^2$  (compare section 4.4), it is shown that  $\sigma_{\text{tot}}$  is still dominated by the statistical uncertainty  $\sigma_{\text{stat}} = 0.108 \text{eV}^2$ . The total systematic uncertainty  $\sigma_{\text{syst}} = 0.072 \text{eV}^2$  is smaller by a factor of  $\frac{2}{3}$ . It is dominated by the column density

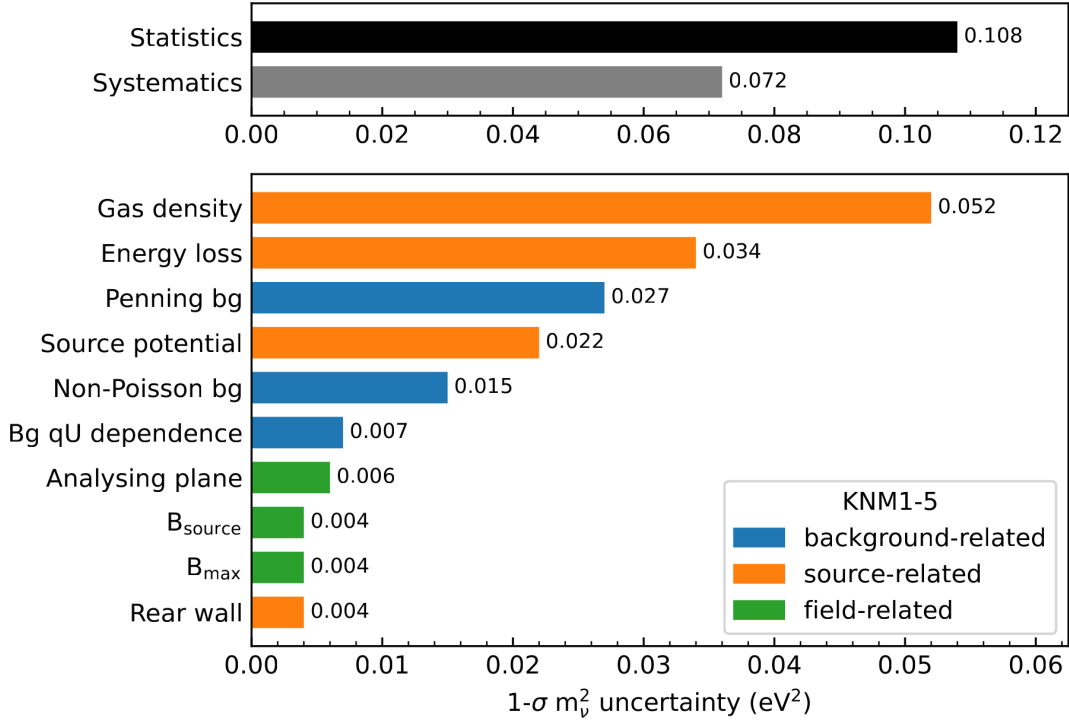


Figure 2.8: The so-called systematics breakdown of the neutrino mass result for the first five KNM campaigns. It shows the impact of the statistical uncertainty  $\sigma_{\text{stat}}$  and the individual systematic uncertainties on the total uncertainty  $\sigma_{\text{tot}}$  on the effective neutrino mass squared  $m_\nu^2$ . Provided by Christoph Wiesinger.

and the energy loss function (compare section 2.3.1). The uncertainties caused by the electromagnetic fields (compare section 2.3.3) are subdominant.

In the following chapters, the status of the KATRIN data collection and the continuation of the neutrino mass analysis for the next four measurement campaigns are presented.



# Chapter 3

## Data Monitoring

The projected sensitivity of the KATRIN experiment on the effective electron anti-neutrino mass is  $m_\nu < 0.3 \text{ eV}$  (90% C.L.) [25], which will be reached by the end of 2025 after  $\sim 1000$  measurement days. As introduced in section 2.5, the current KATRIN neutrino mass result is still dominated by the statistical uncertainty (see figure 2.8). The number of collected electrons in the 40 eV analysis window used for this most recent result is  $\sim 36 \cdot 10^6$  (see figure 3.1). By the end of the 9th measurement campaign, this number increased to  $\sim 98 \cdot 10^6$ , corresponding to about a factor of 2.7 more statistics. The analysis of these next four campaigns is presented in this thesis. With the last completed measurement campaigns as of August 2024 (KNM10-13), the number of collected electrons was increased by another factor of approximately 1.6 to  $\sim 157 \cdot 10^6$ . The final KATRIN neutrino mass result with about  $200 \cdot 10^6$  collected electrons is expected to be dominated by the systematic uncertainty.

To monitor the data quality of the currently ongoing  $\beta$ -scans, a web interface called

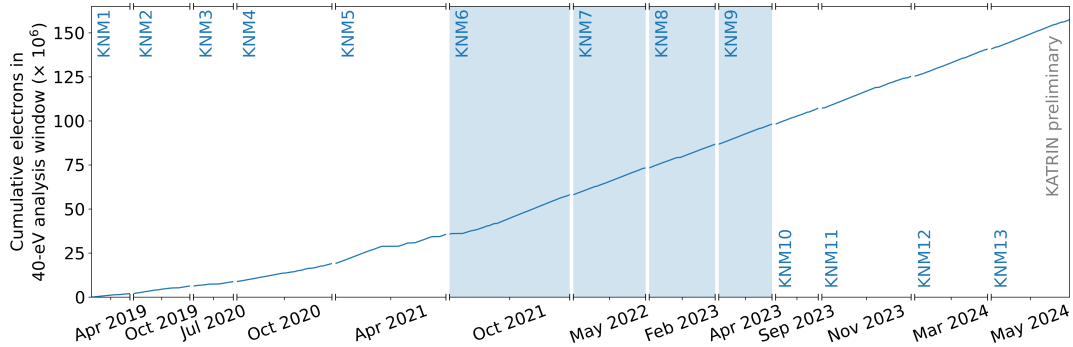


Figure 3.1: The total number of collected electrons in the 40 eV analysis range for the first 13 KNM campaigns. For the campaigns KNM6-9 (blue filled), the neutrino mass analysis is presented in this thesis. The data of KNM11-13 still has to undergo a quality check.

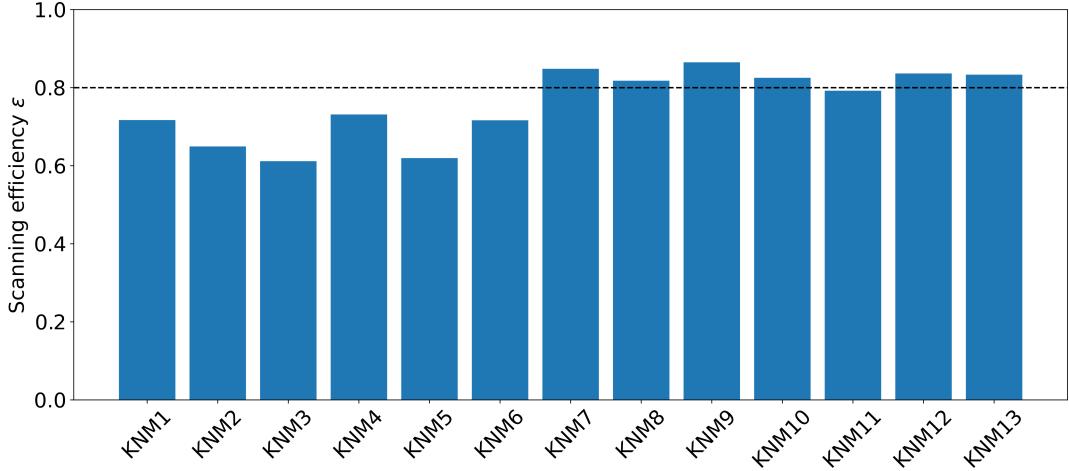


Figure 3.2: Scanning efficiency  $\epsilon$  of every KNM campaign. The improvement of  $\epsilon$  towards later campaigns suggests that the priority moved from optimizing the setup to gathering statistics.

*Webtrium*<sup>1</sup> was developed by Dr. Christian Karl et al. During this thesis, *Webtrium* was expanded to also monitor the collection of statistics and the measurement efficiency of the currently ongoing KNM campaign since an efficient statistics collection is essential to reach the best sensitivity by the end of the KATRIN experiment. The new functions were first used for the campaign KNM12, which started in January 2024. In figure 3.2, the scanning efficiency  $\epsilon$  of every KNM campaign is shown. For that, every time  $t_i$  spent collecting neutrino mass data at a retarding voltage set point  $U_i$  is summed up and divided by the total measurement time  $t_{\text{tot}}$ , which is the time between the start of the first and the end of the last  $\beta$ -scan:

$$\epsilon = \frac{1}{t_{\text{tot}}} \sum_i t_i \quad (3.1)$$

The sum over all measurement times  $t_i$  in equation 3.1 does not include the time between the individual  $qU_i$  points, which is used to change the voltage  $U$ . Furthermore, the time spent on systematic measurements or faulty scans is also not included in the sum.

In figure 3.2, it can be seen that for the first six KNM campaigns, the scanning efficiency was always lower than 80%. Since KNM7, it has always been higher than that, except for KNM11. This indicates a focus shift to statistics collection rather than setup optimization after KNM6.

<sup>1</sup><https://webtrium.edm.nat.tum.de/>

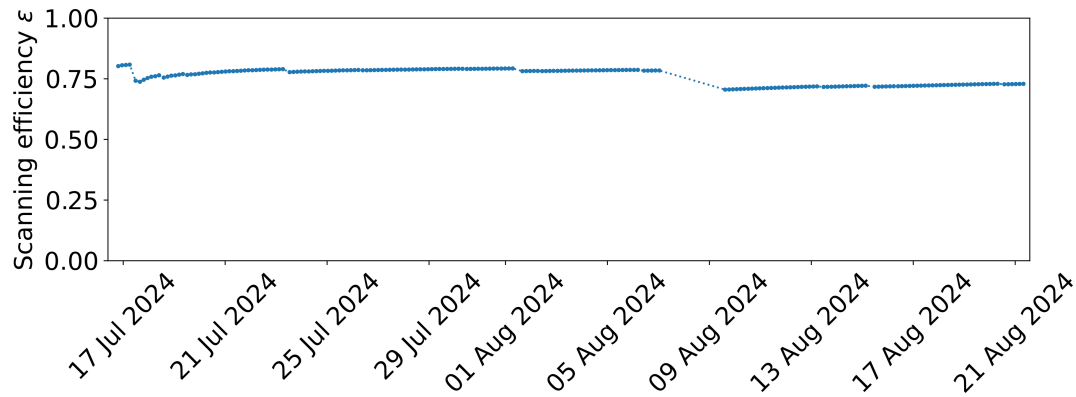


Figure 3.3: Display of the efficiency monitoring on the *Webtrium* web page, with the currently ongoing measurement campaign KNM14 as an example. The reason for the data gap around 7 August was a broken air coil.

Figure 3.3 shows how the efficiency monitoring on the *Webtrium* web page is displayed, with the currently ongoing measurement campaign KNM14 as an example. Data taking interruptions are clearly visible by dips. This enables the monitoring of the measurement efficiency in nearly real-time, as described above.



## Chapter 4

# Analysis of the 6th to 9th KATRIN campaigns

The last published KATRIN neutrino mass result [25], based on the data of the first five KNM campaigns, was introduced in section 2.5. As of August 2024, 13 measurement campaigns have been completed, and the data-taking will be pursued until the end of 2025. In this chapter, the continuation of the neutrino mass analysis for the next four campaigns (KNM6-9) is presented. It starts with the data selection, where the determination of the for the analysis used  $\beta$ -scans and detector pixels and patches is explained. After that, the used systematic input parameters are introduced. Then, data quality investigations are presented, where the stability of the fit parameters and the impact of different scanning directions are examined. In the end, the so-called twin analysis with its systematics breakdowns is presented, and the neutrino mass sensitivity of the 6th to 9th KATRIN campaigns is obtained.

### 4.1 Data selection

As described in section 2.2.4, every KNM campaign consists of a few hundred  $\beta$ -scans, each of which is an individual measurement of the integral tritium spectrum. Furthermore, every pixel of the FPD also measures its own spectrum. The different possibilities to combine this data for the neutrino mass analysis are discussed in section 2.4.2. As a first step of the analysis, the quality of the data has to be checked. That means it has to be decided which  $\beta$ -scans and which pixels and related to that, which patches are used for the analysis. These processes will be described in the following sections.

#### 4.1.1 $\beta$ -scan selection

In chapter 3, the data monitoring tool *Webtrium* was introduced. Among other applications, it was developed to monitor the data taking of the ongoing measurement campaign. After the completion of a KNM campaign, the  $\beta$ -scans, which drew attention to the monitoring tools, are again reviewed by dedicated experts, who

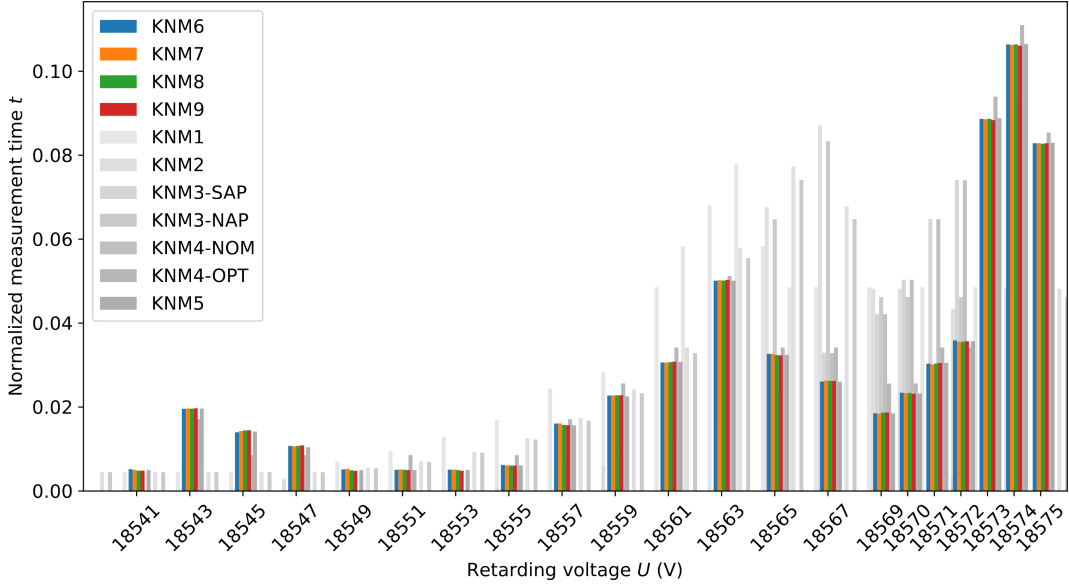


Figure 4.1: The actual, i.e. the measured MTD for the stacked KNM campaigns 1 to 9 in the 40 eV analysis range and without the background set points ( $qU \gtrsim E_0$ ). The measurement times  $t$  for every retarding voltage set point  $U$  were normalized to the total measurement time of every campaign, respectively. Only a slight deviation between the MTDs for KNM5 to KNM9 is visible. The MTDs for previous campaigns show a large difference, not only in the measurement times but also in the voltage set points.

decide if the data can be used for the neutrino mass analysis. This process is called run selection.

One essential feature of the KATRIN neutrino mass analysis is the measurement time distribution (MTD). As described in section 2.2.4, the MTD defines how much time  $t_{\text{MTD}}$  is spent at each retarding voltage set point  $U_{\text{MTD}}$ . The actual, i.e. the measured MTD, can deviate from the set one for the individual  $\beta$ -scans by the accuracy with which the voltage points can be hit and the time it takes until the set point is reached. This impacts the data combination regarding the stacking of the individual  $\beta$ -scans, which is explained in section 2.4.2. Figure 4.1 shows the actual stacked MTDs for the campaigns KNM1-9, respectively. It can be seen that the MTD was changed several times since the start of data taking to achieve a better neutrino mass sensitivity. One of these changes during the campaign KNM4, together with changing experimental parameters, led to a bias in the rate estimation [25]. Because of that, for the neutrino mass analysis, KNM4 had to be split into two separate campaigns with different MTDs (KNM4-NOM and KNM4-OPT for nominal and

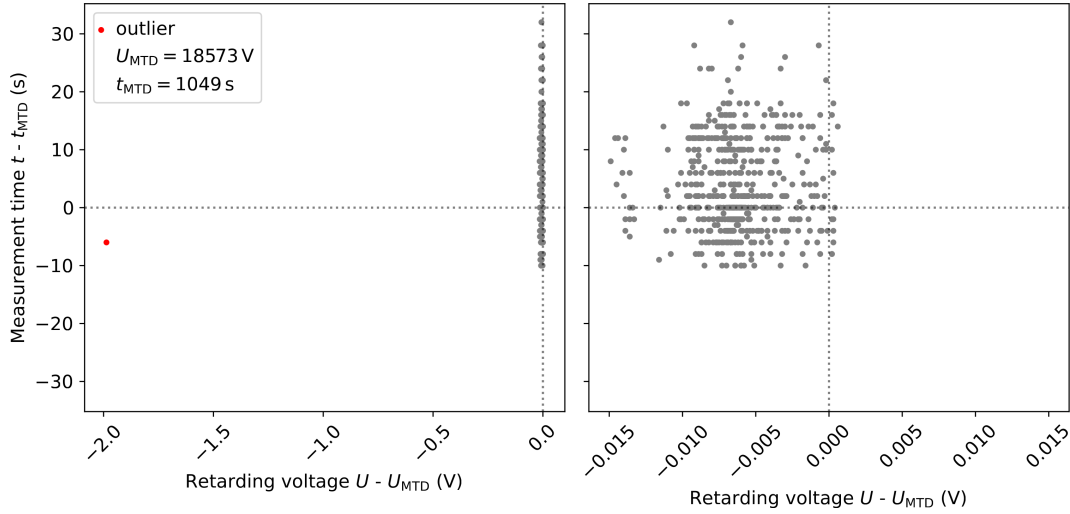


Figure 4.2: This figure shows the difference between the actual measurement time  $t$  and the to-be-set one  $t_{\text{MTD}}$  plotted against the difference between the actual, i.e. the measured retarding voltage  $U$  and the to-be-set one  $U_{\text{MTD}}$  for one so-called subrun with  $U_{\text{MTD}} = 18573$  V and  $t_{\text{MTD}} = 1049$  s for all  $\beta$ -scans of the campaign KNM6. In the left plot, the outlier (red) with a voltage difference of nearly 2 V is clearly visible. The corresponding  $\beta$ -scan was rejected for the neutrino mass analysis. The data for all approved KNM6  $\beta$ -scans is shown in the right plot. The maximum voltage difference here is  $\approx 15$  mV.

optimized MTD, respectively). As visible in figure 4.1, the MTD was not changed anymore since KNM5<sup>1</sup>. Nevertheless, it is important to investigate the actual, i.e. the measured MTD compared to the one to be set, for every individual  $\beta$ -scan.

During the work of this thesis, the actual MTDs, i.e. the measured voltage set points  $U$  and also the measurement times  $t$  for the campaigns KNM6-9, were investigated for every individual  $\beta$ -scan. Figure 4.2 shows the outcome of this study for one MTD set point of the campaign KNM6 as an example. An outlier with a voltage difference of nearly 2 V is clearly visible. The corresponding  $\beta$ -scan was rejected for the neutrino mass analysis. Generally, the deviations between the actual voltage points  $U$ , and the to-be-set ones  $U_{\text{MTD}}$  in the 40 eV analysis range are in the order of 10 mV.

The described investigations lead to a new criterion for the run selection: For the retarding voltage set points  $U$ , a soft limit<sup>2</sup> of 0.05 V difference between the

<sup>1</sup>regarding the 40 eV analysis range

<sup>2</sup>Soft limit here means that not every run which exceeds this threshold is consequently rejected. But it triggers a more detailed quality investigation.

measured and the set value was established. The  $\beta$ -scan corresponding to the outlier in figure 4.2 was the only one rejected by this criterion during the run selection for the campaigns KNM6-9. It should be mentioned that for the campaigns KNM8 and 9, there will be a new, updated high voltage calibration applied, which will change the retarding voltage values a little. Since the observed differences of the actual and the set measurement times  $t$  were in the order of  $10^2$  s, no additional run selection criterion for  $t$  was introduced.

Table 4.1 shows the number of all approved  $\beta$ -scans for the campaigns KNM6-9, respectively, after the successful run selection.

KNM campaign	6	7	8	9
Number of $\beta$ -scans	530	378	332	284

Table 4.1: Number of approved  $\beta$ -scans of the campaigns KNM6-9, respectively, for the neutrino mass analysis.

#### 4.1.2 Pixel and patch selection

As mentioned in section 2.4.2, every pixel of the FPD measures its own integral  $\beta$ -decay spectrum. Unfortunately, not all 148 pixels provide data as expected. For some of them, the monitoring systems indicate instabilities in the electromagnetic fields or source parameters, and some pixels are shadowed by the structural material of the beamline [25, 64]. The data of these so-called inactive pixels has to be rejected for the neutrino mass analysis. This process is called pixel selection and is based on data obtained from  $\beta$ -scans, Krypton and RW calibration measurements [65].

Since the selection and distribution of the inactive pixels depends on the relative alignment between the detector and the electromagnetic fields, it can change, e.g. with the temperature or after mechanical movement of the FPD. There are, in total, five different pixel selections used for the KATRIN neutrino mass analysis: For the KNM campaigns 1, 2, 3-6, 7 and 8-9, respectively (see table 4.2). The pixel selections for the KNM campaigns 3-9 are shown in figure 4.3.

With the pixel selection, the so-called patch selection has to be carried out: Pixels with similar electromagnetic properties are grouped into different patches because the radial inhomogeneities of the magnetic field in the analyzing plane  $B_{\min}$  and the retarding potential  $qU$  are too large to use the uniform pixel combination for the neutrino mass analysis when using the SAP measurement configuration (compare section 2.3.3). The patch selection includes four steps (see [64] for more details):

1. The pixel-wise values for the magnetic field in the analyzing plane  $B_{\min}$  and the retarding potential offset  $qU_{\text{off}}$  are determined from Krypton calibration measurements (see figure 4.4). The offset alters the retarding potential  $qU$ ,

KNM campaign(s)	Number of active pixels (pixel numbers)
1	117 (0-96, 101-109, 113-120, 131-133)
2	117 (0-96, 99, 101-109, 114-120, 131-133)
3-6	126 (0-99, 101-111, 114-122, 130-133, 143-144)
7	123 (0-99, 101-111, 114-116, 118-122, 131-133, 144)
8-9	125 (0-99, 101-111, 114-122, 131-133, 143-144)

Table 4.2: Number of active pixels and their pixel numbers for every KNM campaign from 1 to 9.

which electrons have to overcome to get counted by the pixel:  $qU \rightarrow qU + qU_{\text{off}}$ . For the magnetic field of the source  $B_S$  (2.52 T), the maximum magnetic field  $B_{\text{max}}$  (4.24 T) and the retarding energy  $qU$  (18.6 keV), which is applied to the MS, one value is used respectively for all pixels.

2. The simplified transmission function  $T(E)$ <sup>3</sup>, i.e. without scattering effects and synchrotron radiation losses (equation 2.12) is calculated for every pixel (see figure 4.5).
3. For every transmission function  $T(E)$ , the energy  $E_{1/2}$ , where  $T(E)$  reaches the half of its maximum, is calculated (compare figure 4.5).
4. All pixels are sorted by their values for  $E_{1/2}$  and grouped into 14 patches (this will be explained in more detail in the following). The results for the patch selections of KNM7 and KNM8-9 are shown in figure 4.6.

The described procedure of the patch selection is well established since KNM3. KNM3-SAP was the first measurement campaign using the SAP setting as described in section 2.3.3, which necessitated grouping pixels into patches for the neutrino mass analysis. For the campaigns KNM3-5, it was decided to use 14 patches because the pixels could then be distributed uniformly into patches with 9 pixels each. Since KNM6 has the same pixel selection as KNM3-5 (see table 4.2), also for this campaign, the same patch selection is used. However, this is no longer possible for the campaigns KNM7-9 (see table 4.2). An adjustment of the last step (4.) of the patch selection was made, where an additional criterion was introduced: To have enough statistics in every patch, they must include at least 8 pixels. With this new criterion, the sum of the patch-wise variances  $\sigma_{E_{1/2}}^2$  has to be minimized. The results of the patch selection for the campaigns KNM7 and KNM8-9 are shown in figure 4.6.

In the future, the plan is to optimize the patch selection process much further. During this work, first studies indicated that using a smaller number of patches,

<sup>3</sup>Here, the transmission function  $T$  depends only on the electron energy  $E$ , because the retarding potential  $qU$  is fixed.

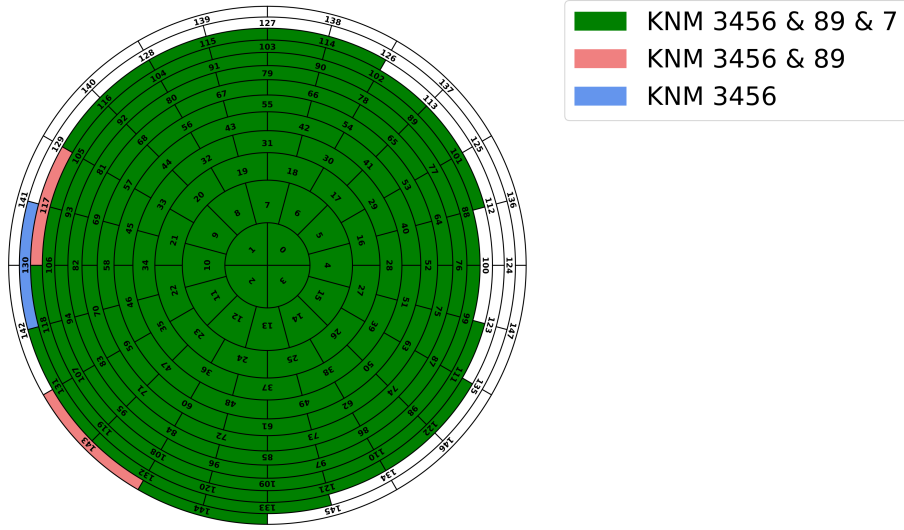


Figure 4.3: Sketch of the FPD with its 148 pixels. The active pixel selections of the KNM campaigns 3-9 are shown in colours. For KNM3-6, the data of the green, red and blue pixels is used. For KNM7, only the green pixels are active. For KNM8-9, the data of the green and red pixels is used. The white pixels are inactive for all of the KNM3-9 campaigns. Provided by Jaroslav Štorek.

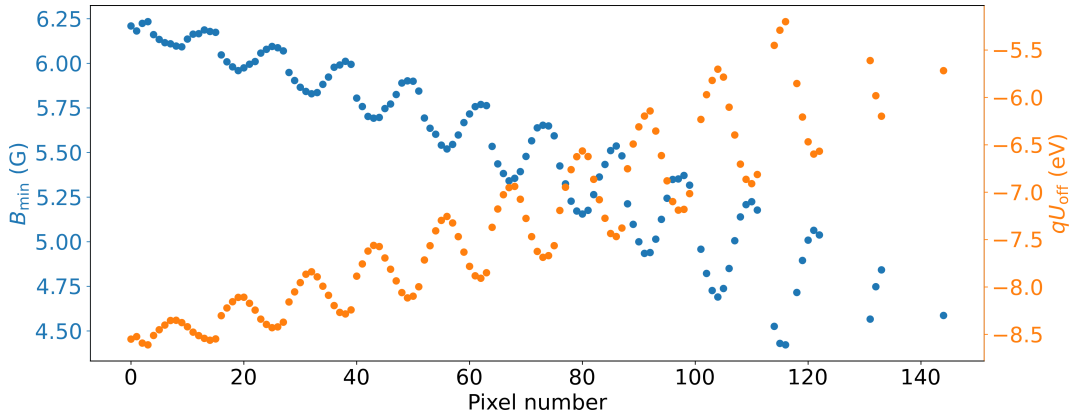


Figure 4.4: Pixel-wise values for the magnetic field in the analyzing plane  $B_{\min}$  (blue) and the retarding potential offset  $qU_{\text{off}}$  (orange), which are determined from Krypton calibration measurements for the campaign KNM7. A misalignment of  $\mathcal{O}(1\text{mm})$  between the detector wafer and the beamline axis leads to the oscillatory pattern of the parameter values [25].

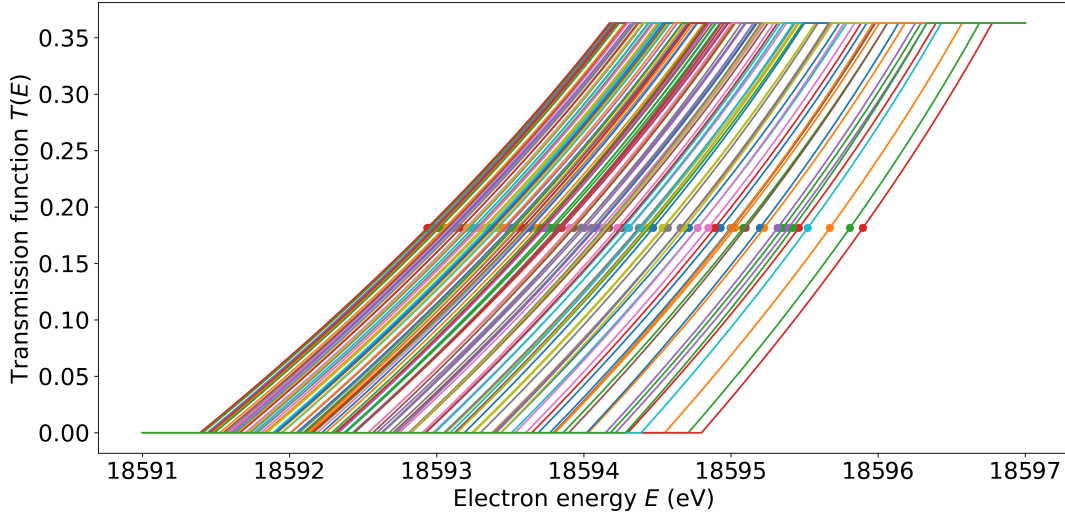


Figure 4.5: Second step of the patch selection: Calculated pixel-wise, simplified transmission functions  $T(E)$  (lines), i.e. without scattering effects and synchrotron radiation losses (equation 2.12). The third step of the patch selection: For every transmission function, the energy  $E_{1/2}$ , where  $T(E)$  reaches half of its maximum, is calculated (dots).

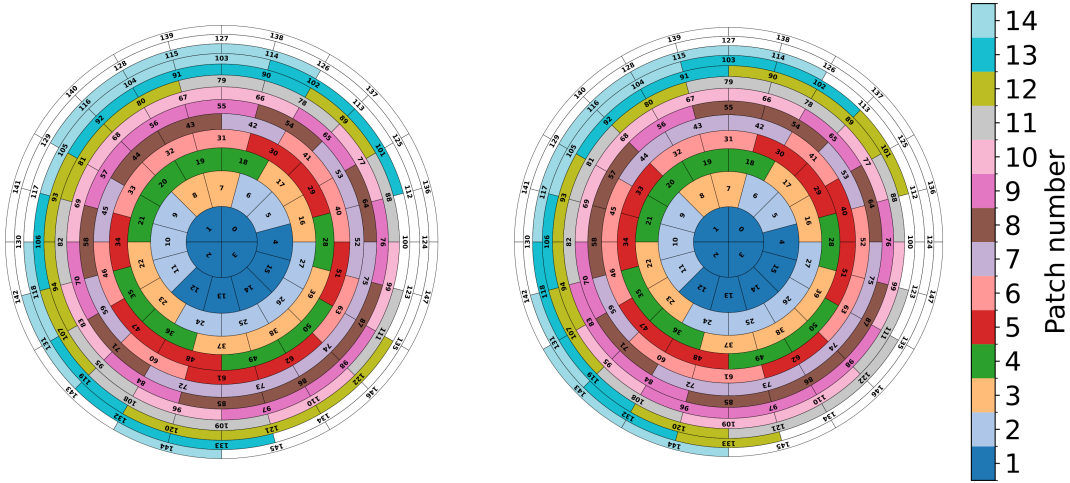


Figure 4.6: Results of the patch selection for the campaign KNM7 (left) and KNM8-9 (right). The data of the white (inactive) pixels is not used for the neutrino mass analysis. A misalignment of  $\mathcal{O}(1 \text{ mm})$  between the detector wafer and the beamline axis is the reason for the not perfectly ring-wise patches [25].

i.e. more pixels per patch with then more significant difference between the individual electromagnetic properties, leads to a relatively small bias on the neutrino mass squared  $m_\nu^2$  and also the sensitivity on it decreases only a little. The idea is to optimize the grouping algorithm so that the loss of sensitivity on  $m_\nu^2$  gets negligible while simultaneously reducing the number of patches. This would lead to a computational advantage since the number of model evaluations during the analysis would decrease (compare section 2.4.2).

## 4.2 Systematic input parameters

As described in section 2.3, the systematic effects of the KATRIN experiment with their uncertainties are crucial for the neutrino mass analysis. The treatment of these is described in section 2.4.3. Dedicated teams within the KATRIN collaboration carry out the determination of the systematic input values and their uncertainties. This was no task of this thesis. Unfortunately, not all of the systematic inputs were ready by the time of this work. To be able to already start the neutrino mass analysis for the campaigns KNM6-9 anyway, to obtain first preliminary results, placeholder values were used for the systematic inputs. These mimic the expected systematic effects in a realistic way to receive first estimations for the neutrino mass analysis. In the following, all placeholder inputs are listed (see table 4.3), and it is explained how the values were estimated.

- **Column density (CD):** For the CD  $\rho d$  of the campaigns KNM7-9, respectively, 75 % of the the design value of  $5 \cdot 10^{21} \text{ m}^{-2}$  [28] was assumed. The CD team provided the placeholder uncertainty values as first estimations.
- **Source plasma long-term fluctuations:** The variance  $\sigma_{\text{long-term}}^2$  due to long-term fluctuation of the source plasma is set to zero for the campaigns KNM7-9. Its uncertainty was conservatively estimated to  $0.001 \text{ eV}^2$ , since for the previous SAP campaigns KNM4-6, this value was smaller than  $0.0009 \text{ eV}^2$ .
- **Rear wall (RW):** There are three systematic parameters connected with the rear wall, as explained in section 2.3.1, the rear-wall endpoint  $E_{0,\text{RW}}$ , the rear wall FSD shape and the rear wall activity. For the first two inputs, the RW team provided placeholder values for all four campaigns as first estimations. It also determined the placeholder values for the RW activity of the campaign KNM6. For the campaigns KNM7-9, respectively, the activity was estimated to be on the same order of magnitude as for KNM5, so the same values are used here as placeholder.
- **Analyzing plane:** These inputs are related to the pixel and patch selection since the values are equal for campaigns with the same pixel and patch se-

KNM campaign	6	7	8	9
Column density	ready	placeholder	placeholder	placeholder
Energy loss	ready	ready	ready	ready
Source plasma <sup>4</sup>	ready	ready	ready	ready
Source plasma long-term fluctuations	ready	placeholder	placeholder	placeholder
Rear wall	placeholder	placeholder	placeholder	placeholder
Background energy slope	ready	ready	ready	ready
Magnetic field of the source	ready	ready	ready	ready
Analyzing plane <sup>5</sup>	ready	ready	placeholder	placeholder
Detector effects	ready	ready	ready	ready

Table 4.3: Status of the systematic inputs used for the neutrino mass analysis of the campaigns KNM6-9 for this thesis. It should be noted that activity fluctuations, the penning background, the background overdispersion and the uncertainties on the FSD are not included in the analysis, as described in section 2.3.

lection, i.e. for the campaigns KNM3-6, KNM7 and KNM8-9, respectively. As placeholder for KNM8-9 the values from KNM3-6 were used, which were adjusted to the pixel and patch selection of KNM8-9 (compare section 4.1.2).

A selection of detailed input values and uncertainties used during the neutrino mass analysis of this thesis can be found in table 1 in the appendix<sup>6</sup>.

### 4.3 Data quality

In section 4.1, the data selection, namely the run, pixel and patch selection, is described. The following steps are quality studies concerning the neutrino mass analysis with the selected data. In this section, the stability of the fit parameters regarding their time and radial evolution and the influence of different scanning directions is discussed.

<sup>4</sup>Here, every effect explained in section 2.3.1 (Source plasma) is contained, except long-term fluctuations  $\sigma_{\text{long-term}}^2$ .

<sup>5</sup>Here, the patch-wise values for  $B_{\text{min}}$ ,  $B_{\text{max}}$  and  $qU_{\text{off}}$  are contained.

<sup>6</sup>All input values and uncertainties can be found here: <https://nuserv.uni-muenster.de:8443/aschwemm/knm-inputs.git> with the commit 771fd0d6

### 4.3.1 Fit parameter stability

As described in section 2.4.1, the free parameters  $\vec{\theta}_{\text{free}}$  of the KATRIN model  $\mu$  from equation 2.25 are the effective neutrino mass squared  $m_\nu^2$ , the endpoint energy  $E_0$ , the normalization factor  $A$  and the background rate  $B$ . The following studies on the parameter stability are performed for  $E_0$ ,  $A$  and  $B$ , not for  $m_\nu^2$  since it should remain blinded to prevent any self-bias of the analysis teams (compare section 4.4.1).

The evolution of the endpoint  $E_0$  is crucial for the neutrino mass analysis since instabilities of  $E_0$  lead to an additional broadening of the model. If this is not taken into account,  $m_\nu^2$  gets shifted to more negative values (see [66] for more details). The normalization factor  $A$  is also important because instabilities there hint at incomplete knowledge of the activity parameters [34], e.g. the column density. The background rate  $B$  is not as substantial as  $E_0$  and  $A$  since it averages out as a linear parameter [34], but it is also discussed here for completeness reasons.

### Time evolution

To investigate the time evolution of the free fit parameters, a uniform (see section 2.4.2) fit<sup>7</sup> is performed for every  $\beta$ -scan individually and with statistical uncertainty only. The effective neutrino mass is fixed to zero ( $m_\nu = 0$  eV). These so-called run-wise fits are shown in figure 4.7. The parameter values are fitted to a linear function to look for time-dependent trends. The results of the described investigations are summarized in figure 4.8.

The endpoint  $E_0$  shows a jump between the campaigns KNM6 and KNM7 (see figure 4.8) and also in the beginning of KNM8 (see figure 4.7). These jumps can be explained by the changes of the RW bias voltage, which alters the starting potential of the  $\beta$ -electrons as described in section 2.1.1. These changes are shown in figure 4.9. The RW voltage adjustments are used to counteract radial dependencies of the endpoint  $E_0$ , which will be discussed later in this section. The bias voltage should compensate for the work function difference between the RW and the beam tube surfaces. When both are at the same potential, the electric potential in the source is the most homogeneous, radially and longitudinally [67].

Furthermore, the linear fits to the run-wise  $E_0$  values indicate a slight endpoint drift for all four campaigns (see figure 4.8), which, on the one hand, can again be explained by the change of the RW bias voltage and on the other side by time-dependent source plasma instabilities as described in section 2.3.1. This drift can be included in the neutrino mass analysis by the additional broadening  $\sigma_{\text{long-term}}^2$  of the model. An estimation for  $\sigma_{\text{long-term}}^2$  is given by the overdispersion of  $E_0$ . These values are summarized in table 4.4. It should be noted that these estimations are

---

<sup>7</sup>For the fits of the data quality studies *Fitrium* was used (see section 2.4.4).

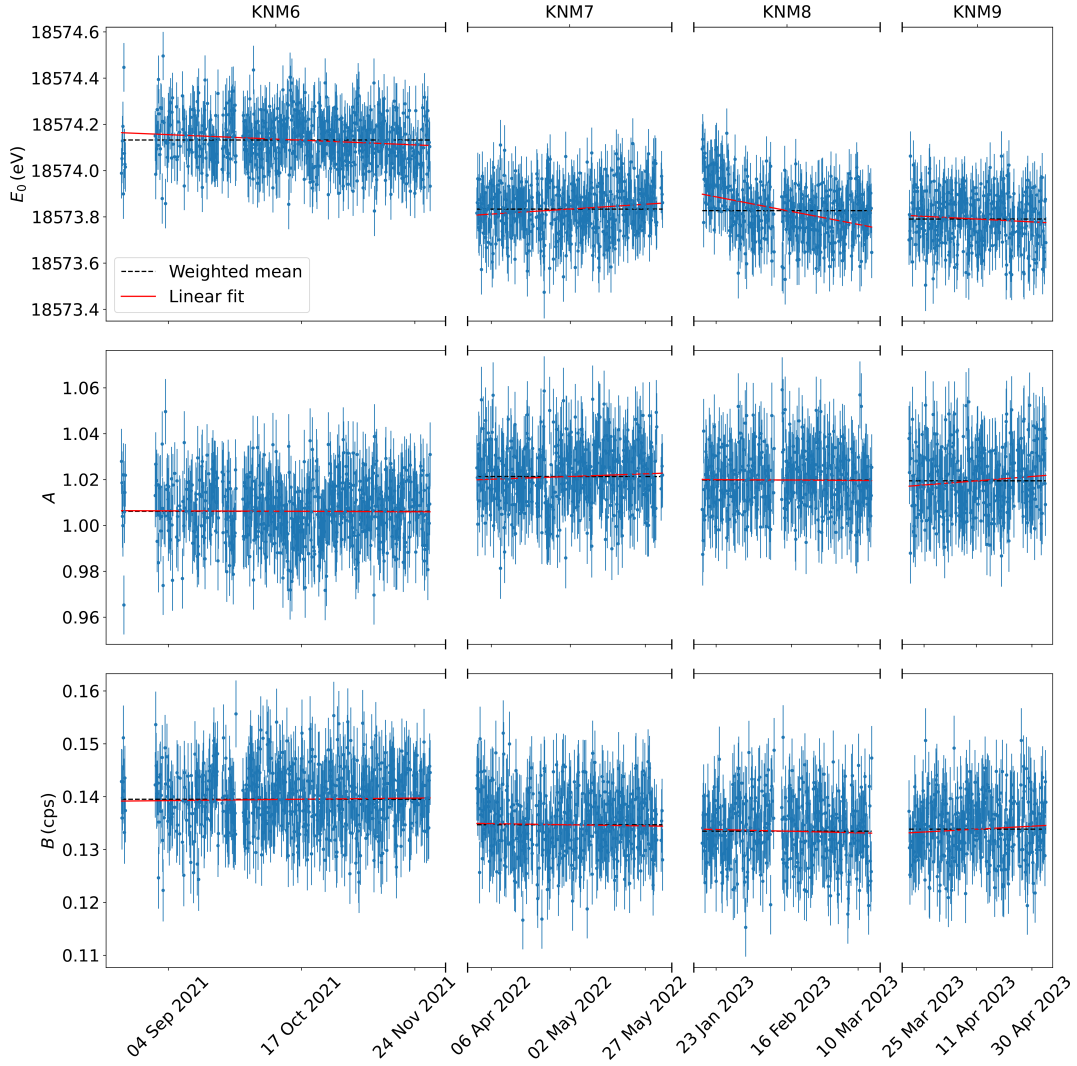


Figure 4.7: The time evolution of the endpoint  $E_0$  (top), the normalization factor  $A$  (middle) and the background rate  $B$  (bottom) for the campaigns KNM6-9. Every  $\beta$ -scan is fitted individually using the data from the 40 eV analysis range and with statistical uncertainty only. The uniform pixel combination is used, where the measured counts of all active pixels are summed up. The effective neutrino mass is fixed to zero ( $m_\nu = 0$  eV). To look for temporal trends, a linear fit (red) to the blue parameter values is performed for every campaign and every fit parameter. The reason for the data gap at the beginning of KNM6 is a cooling problem, which appeared at that time.

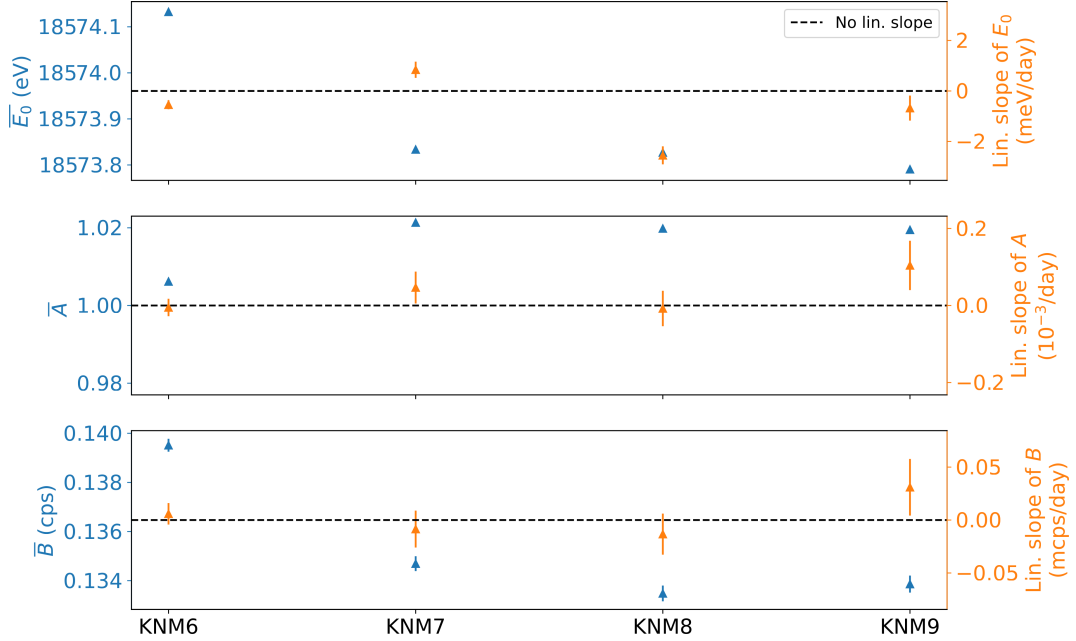


Figure 4.8: Summary of the data quality investigations regarding the time evolution of the free fit parameters  $E_0$  (top),  $A$  (middle) and  $B$  (bottom). The values of the weighted means are shown in blue. The error on the weighted mean is  $\sqrt{\sum_i \sigma_i^2}$  with the individual standard deviations  $\sigma_i$ . The fitted linear slope values are shown in orange. The jump of the weighted mean of the endpoint  $\overline{E}_0$  between the campaigns KNM6 and KNM7 can be explained by the RW bias voltage change between these campaigns (see figure 4.9). It changes the starting potential of the  $\beta$ -electrons. Also, for the normalization factor  $\overline{A}$  and the background rate  $\overline{B}$ , a jump after KNM6 is visible. This is considered since the individual measurement campaigns are separated during the analysis as shown in equation 2.33. The linear slopes of  $E_0$  hint at a small endpoint drift for all four campaigns. This can be included in the analysis by an additional broadening of the model. For  $A$  and  $B$  no significant temporal drifts are visible.

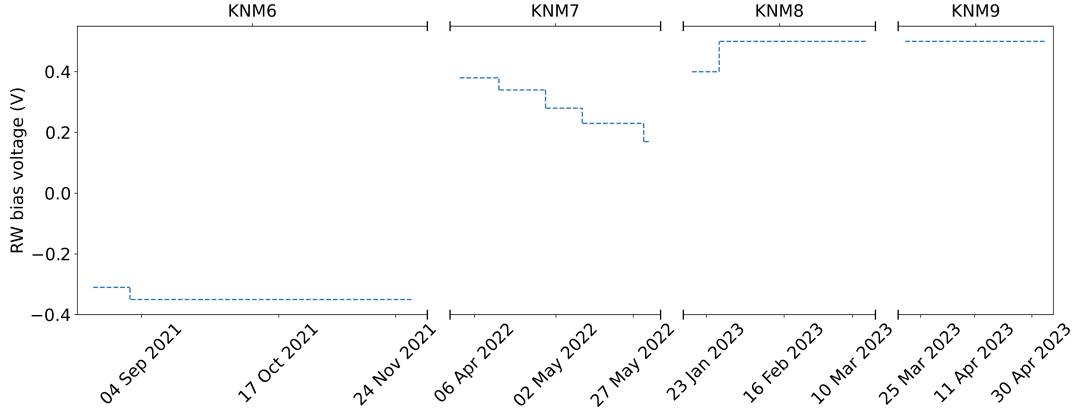


Figure 4.9: The RW bias voltage for the campaigns KNM6-9. The voltage changes are due to counteracting radial dependencies of the endpoint  $E_0$  [67]. These adjustments have an impact on the fitted endpoint energy  $E_0$  (compare figures 4.7 and 4.8) since the starting potential of the  $\beta$ -electrons gets altered.

KNM campaign	6	7	8	9
Overdispersion of $E_0$ ( $\text{meV}^2$ )	$176 \pm 708$	$-164 \pm 853$	$1873 \pm 974$	$666 \pm 918$

Table 4.4: Overdispersion values of the run-wise endpoint energy  $E_0$  as an estimation for the additional broadening  $\sigma_{\text{long-term}}^2$ , which has to be included into the neutrino mass analysis because of temporal endpoint drifts. The quoted uncertainties are determined via the bootstrapping method [69].

not used in the final analysis, but the determination procedure of  $\sigma_{\text{long-term}}^2$  is similar [68].

The normalization factor  $A$  shows a small jump ( $\mathcal{O}(10^{-2})$ ) between the campaigns KNM6 and KNM7 and is stable for KNM7-9. Also, the deviation from the expected value of 1.0 is rather small ( $\mathcal{O}(10^{-2})$ ). No significant temporal drifts are visible for  $A$  and the background rate  $B$ . The mean background rate decreases after KNM6 and is then stable for KNM7-9. The overdispersion values for  $A$  and  $B$  are summarized in the appendix in table 2.

## Radial evolution

In addition to the time evolution, the radial dependency of the fit parameters can be investigated. For that, every detector patch is fitted individually for the stacked runs of a KNM campaign and again with statistical uncertainty only and the effective neutrino mass fixed to zero ( $m_\nu = 0 \text{ eV}$ ). It should be noted that the patch-wise

KNM campaign	6	7	8	9
Linear slope of $E_0$ (meV/patch)	$-2.8 \pm 0.8$	$-0.9 \pm 1.0$	$-5.2 \pm 1.0$	$-2.9 \pm 1.1$

Table 4.5: Values of the linear slopes, fitted to the patch-wise endpoint  $E_0$  fit values, for the campaigns KNM6-9, respectively.

evolution is not a perfect radial evolution since the patches are not equal to the detector rings, as shown in figure 4.6.

These so-called patch-wise fits are shown in figure 4.10 for the endpoint  $E_0$ . The parameter values are fitted to a linear function to recognise radial trends. The values of their slopes are summarized in table 4.5. The campaign KNM7 shows a vanishing radial  $E_0$  dependency, while for KNM6, KNM8 and KNM9, a clear patch-wise trend for  $E_0$  is visible. As already mentioned before, the reason for these dependencies are plasma inhomogeneities, which should be minimized by RW bias voltage adjustments.

Since the final neutrino mass analysis is carried out for each detector patch individually, smaller deviations between the fit parameters are not crucial. Nevertheless, looking at these trends to spot apparent misbehaviour is important. In the appendix, the patch-wise fits for the normalization factor  $A$  and the background rate  $B$  are shown in figures 1 and 2. The values of their patch-wise slopes are summarized in the appendix in table 3.  $A$  decreases, and  $B$  increases to the outer part of the detector as expected.

### 4.3.2 Scanning directions

Another quality study, which was performed in the scope of this thesis, was the dependency of the fit parameters on different scanning directions. As described in section 2.2.4, during a  $\beta$ -scan, the retarding voltage  $U$  is swept across a fixed set of up to 40 set points, which is defined by the MTD. There are three different orderings in which these voltage points alternately are set:

- **Up:** The retarding voltage is constantly increasing.
- **Down:** The retarding voltage is constantly decreasing.
- **Random:** The retarding voltage is changed randomly.

The three different scanning directions are visualized in figure 4.11. It should be mentioned that for every direction, the first two retarding voltage set points are equal.

With this differentiation, the studies described in section 4.3.1, namely the time and radial evolution, are repeated for separated data sets, grouped by the three

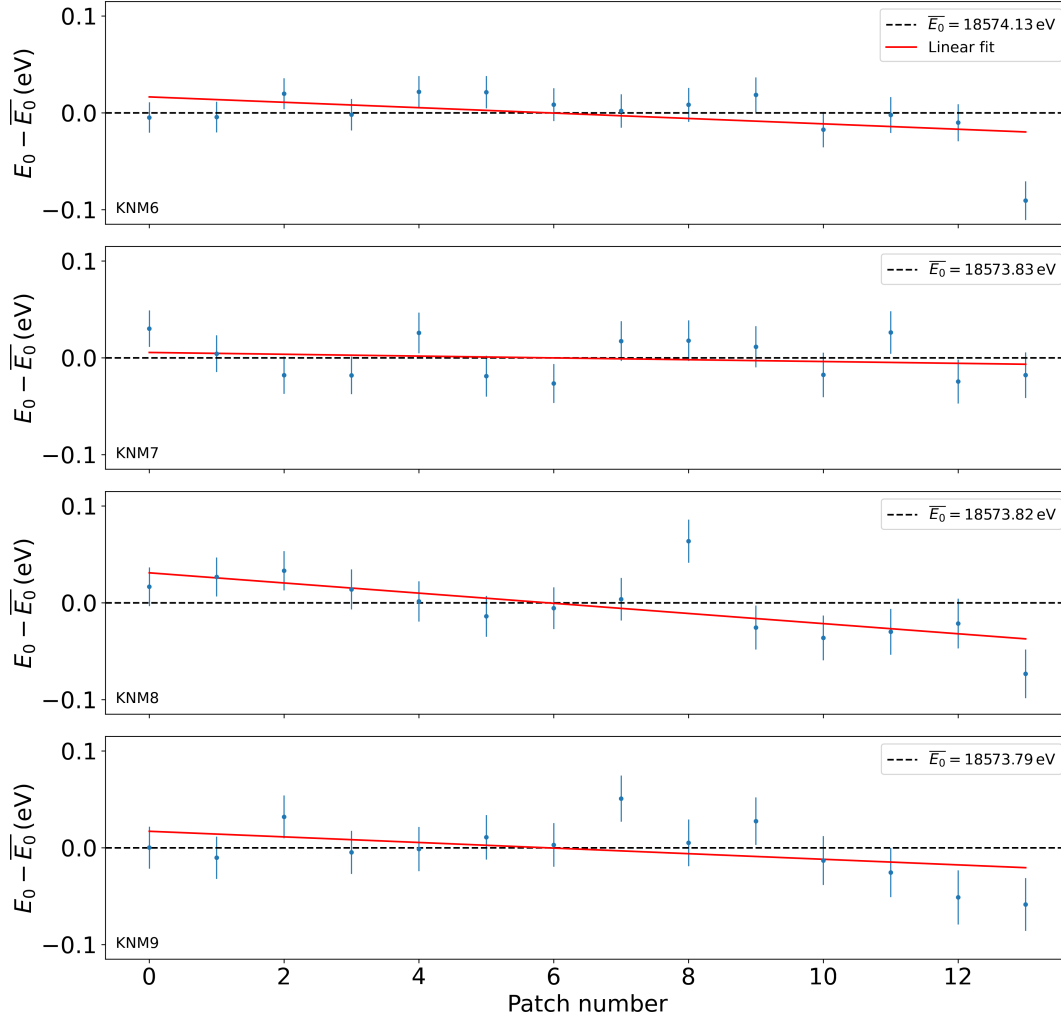


Figure 4.10: Patch-wise evolution of the endpoint  $E_0$  for the campaigns KNM6-9, respectively. All runs of a campaign are stacked, and every detector patch is fitted individually, with statistical uncertainty only. The effective neutrino mass is fixed to zero ( $m_\nu = 0$  eV). A linear fit (red) to the blue parameter values is performed for every campaign, respectively.

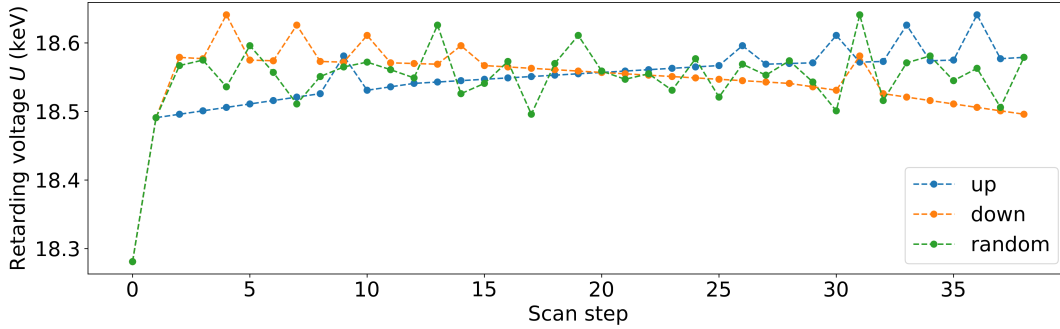


Figure 4.11: The sweeping of the retarding voltage  $U$  during a  $\beta$ -scan is realized by three different scanning directions: Up (blue), down (orange) and random (green). For the up and down direction, respectively, the background voltage points are set in between the smaller set points. This should prevent effects related to constant increasing and decreasing of  $U$ .

possible scanning directions. The results for the endpoint  $E_0$  are summarized in figure 4.12

The weighted mean values of the run-wise endpoint  $\overline{E_0}$  are consistent with the previous results (compare figure 4.8) and agree for all different scanning directions, respectively, without any patterns. The same holds for the run-wise  $E_0$  slope and overdispersion values, although for the campaign KNM9, the variation between the values for the different scanning directions is rather big. But the distribution of the slope values matches the one of the overdispersion values for KNM9, knowing the overall run-wise slope with a value of  $\approx -0.7$  meV/d (compare figure 4.8). The patch-wise  $E_0$  slope values for KNM8 show a more significant deviation between the individual scanning directions since large source plasma instabilities are present, as described before. This can be seen in table 4.5, where the patch-wise slope value of KNM8 is the largest of all campaigns, nearly twice as big as for KNM6 and KNM9, respectively. Nevertheless, this is not problematic because the results for the campaigns KNM6, KNM7 and KNM9 are consistent for the different scanning directions, and overall, no significant pattern is visible.

The results for the normalization factor  $A$  and the background rate  $B$  are shown in figures 3 and 4 in the appendix. Also there, no clear patterns are visible, and the values are consistent with the previous results.

## 4.4 Neutrino mass analysis

The last part of this thesis covers the determination of the statistical and systematic sensitivity on the effective neutrino mass squared  $m_\nu^2$  for the campaigns KNM6-9,

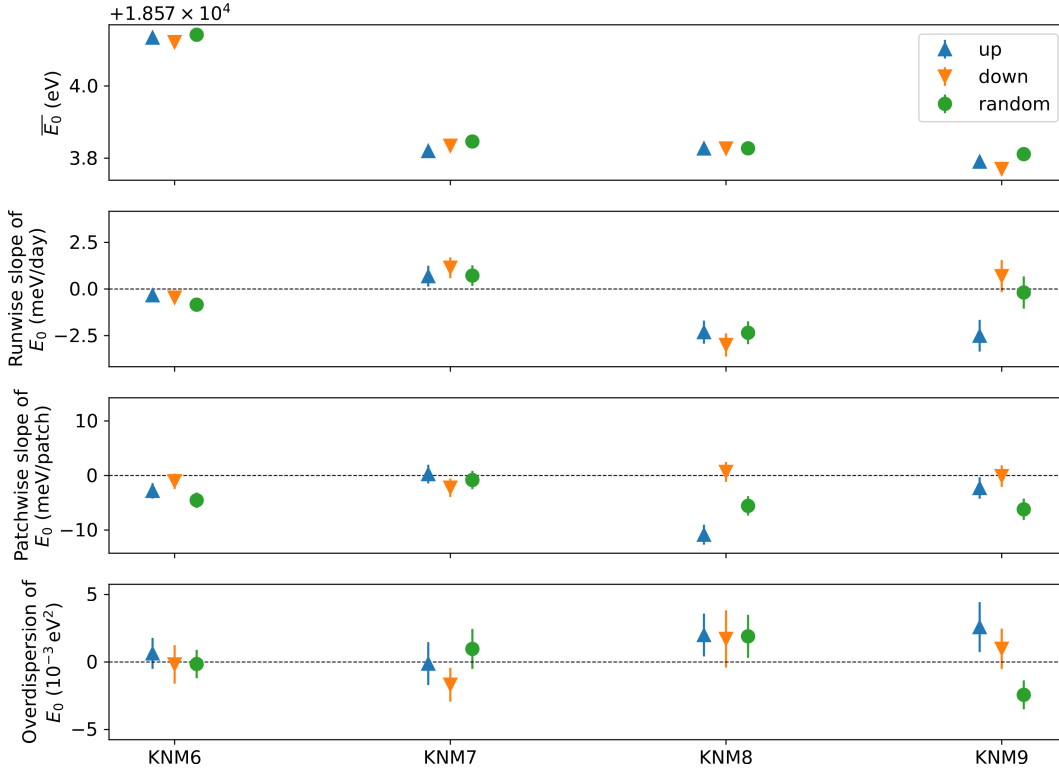


Figure 4.12: Results of the data quality investigations for the endpoint  $E_0$ , regarding the dependency of the fit parameters on different scanning directions of the retarding voltage  $U$ , namely up (blue), down (orange) and random (green). The difference between the individual values for the KNM8 patch-wise  $E_0$  slope can be explained by large source plasma instabilities. Overall, no significant patterns are visible.

respectively, and the impact of the individual systematic effects, described in section 2.3. First, the two-step blinding strategy for the KATRIN neutrino mass analysis is introduced, and then the so-called systematics breakdowns (compare figure 2.8) for the campaigns KNM6-9, respectively, are discussed. In the end, a combined sensitivity estimation is made.

#### 4.4.1 Blinding strategy

The KATRIN collaboration introduced a two-step blinding strategy for the neutrino mass analysis to prevent any self-bias of the analysis teams. The steps of the blinding process are

1. the broadening of the final states distribution (FSD) and

2. the full neutrino mass analysis on simulated KATRIN data.

In the following, these two methods are explained in more detail.

### Broadening of the final states distribution

The so-called final states distribution (FSD) and its impact on the model were introduced in section 2.2.1. Figure 2.4 shows the FSD of molecular tritium  $T_2$ , which is used for the final KATRIN neutrino mass analysis.

As first blinding step, the width of the FSD ground state is changed by an unknown value. This introduces an additional broadening of the model  $\sigma_{\text{blind}}^2$ , which shifts the neutrino mass squared  $m_\nu^2$  by  $\approx -2(\sigma_{\text{true}}^2 + \sigma_{\text{blind}}^2)$ , with the true ground state variance  $\sigma_{\text{true}}^2$  (see [34] for more details).

It should be noted that the blinded FSDs<sup>8</sup> for the campaigns KNM6-9 were used during the data quality studies, presented in section 4.3. This has no impact on the results because the relative evolution of the fit parameters was examined. Other than that, the effective neutrino mass  $m_\nu$  was fixed to zero for these investigations.

### Analysis of simulated KATRIN data

As second step of the blinding strategy, the complete neutrino mass analysis chain is performed with simulated and statistically unfluctuated KATRIN data, so-called twins. For every  $\beta$ -scan, a copy is created, which contains all relevant information of the real scan, i.e. the systematic parameter values, retarding energies and measuring times. For the endpoint energy  $E_0$ , a representative value of 18 573.7 eV is chosen. So-called pixel-wise fits are performed for the values of the normalization factor  $A$  and the constant background rate  $B$ . These are similar to the patch-wise fits described in section 4.3.1, but now, not every patch but every pixel of the detector is fitted individually. The obtained pixel-wise values for  $A$  and  $B$  represent the true values [34] and are shown in figure 4.13 for the campaign KNM6 as an example. The effective neutrino mass is fixed to zero for every twin:  $m_\nu^2 = 0.0 \text{ eV}^2$ .

Now, when carrying out the full neutrino mass analysis on the twins, two types of sanity checks are possible (see [34] for more details):

- For the effective neutrino mass, the true value of  $m_\nu^2 = 0.0 \text{ eV}^2$  has to be recovered.
- The total uncertainty on  $m_\nu^2$  and the impact of the individual systematic components on it has to be consistent with the results from the complementary analysis team.

---

<sup>8</sup>There is one blinded FSD per campaign available, for which the random values for  $\sigma_{\text{blind}}^2$  are different.

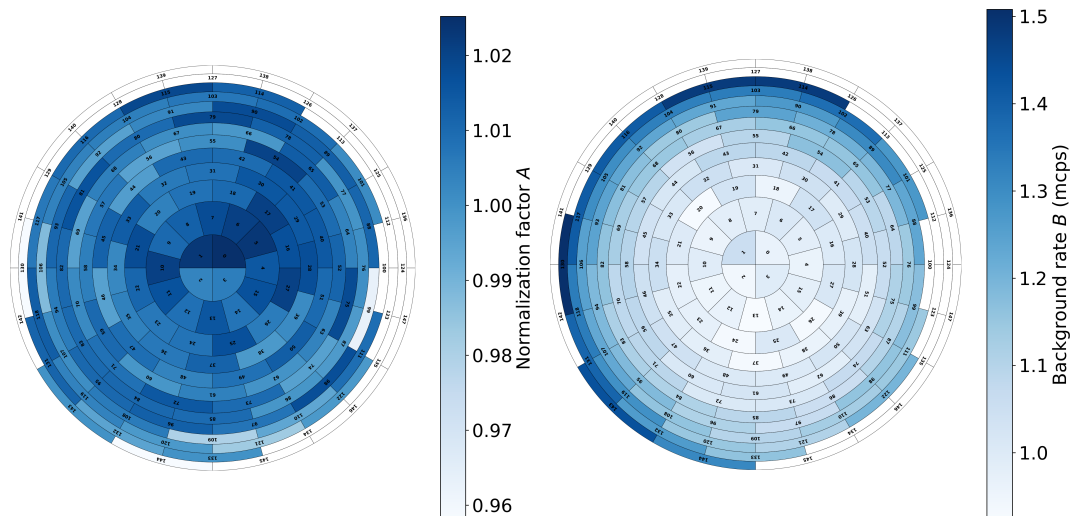


Figure 4.13: Pixel-wise values for the normalization factor  $A$  (left) and the background rate  $B$  (right) for the campaign KNM6, which are used to create simulated and statistically unfluctuated KATRIN data, so-called twins as second blinding step. For that, all runs of the campaign are stacked, and every detector pixel is fitted individually, with statistical uncertainty only and the effective neutrino mass fixed to zero ( $m_\nu = 0$  eV).

When both of the sanity checks are successful, the first unblinding step is carried out: The analysis of the real data but with the broadened FSD. The second unblinding step is the analysis of the real data with the real FSD.

The following results for the campaigns KNM6-9 are based on the twin data. With this analysis, the statistic and systematic sensitivity on the effective neutrino mass squared  $m_\nu^2$  can be determined.

#### 4.4.2 Sensitivity results

Before the neutrino mass sensitivity results for the campaigns KNM6-9, respectively, are presented, the outcome of the first sanity check, described above for the twin analysis, is shown in table 4.6. As explained, the simulated true value of  $m_\nu^2 = 0.0$  eV<sup>2</sup> has to be recovered by the fits<sup>9</sup> with statistical uncertainty only. This is the case for all of the campaigns KNM6-9, respectively. The shown bias values are in the order of  $10^{-3}$  eV<sup>2</sup> or smaller, which is sufficient.

To obtain the statistical uncertainty  $\sigma_{\text{stat}}$  on the effective neutrino mass squared  $m_\nu^2$  for every campaign of KNM6-9, the confidence interval estimation, which is de-

<sup>9</sup>For all fits of this section, *Netrium* was used (see section 2.4.4).

KNM campaign	6	7	8	9
$m_\nu^2$ ( $10^{-3}$ eV <sup>2</sup> )	-0.55	-1.29	-0.38	-1.76

Table 4.6: Outcome of the first sanity check for the neutrino mass analysis on the simulated KATRIN data with  $m_\nu^2 = 0$  eV<sup>2</sup>. This true value is recovered by the fits with statistical uncertainty only for all of the campaigns KNM6-9, respectively.

scribed in section 2.4.1 is used<sup>10</sup>. To receive the total uncertainty  $\sigma_{\text{tot}}$ , all systematic effects are included in the likelihood function via the nuisance parameter method, described in section 2.4.3. The systematic uncertainty  $\sigma_{\text{syst}}$  is then obtained via quadratic subtraction:

$$\sigma_{\text{syst}} = \sqrt{\sigma_{\text{tot}}^2 - \sigma_{\text{stat}}^2}. \quad (4.1)$$

The results are shown in figure 4.14. From KNM6 to KNM9, the statistic uncertainty continuously increases from 0.153 eV<sup>2</sup> to 0.206 eV<sup>2</sup>, since the number of  $\beta$ -scans, i.e. the amount of statistics per campaign continuously decreases (compare figure 3.1 and table 4.1). On the other side, the systematic uncertainty decreases from 0.075 eV<sup>2</sup> for KNM6 to 0.50 eV<sup>2</sup> for KNM7 by a factor of  $\sim \frac{2}{3}$ , and then by another  $\sim 4\%$  between KNM7 and KNM8 (0.48 eV<sup>2</sup>). For KNM9, the systematic uncertainty is roughly the same as for KNM8 ( $< 0.5\%$  difference). The total uncertainty continuously increases from 0.170 eV<sup>2</sup> for KNM6 to 0.212 eV<sup>2</sup> for KNM9 because it is clearly dominated by the statistical uncertainty, respectively.

To better understand the evolution of the systematic uncertainty  $\sigma_{\text{syst}}$ , described above and shown in figure 4.14, a more detailed investigation of  $\sigma_{\text{syst}}$  is needed. This is done via so-called systematics breakdowns (compare figure 2.8), where the impact of the individual systematic effects is examined. The procedure is similar to the one described above for the total systematic uncertainty, but now, not all systematic effects are included in the likelihood function at once, only the one to be investigated. The results are shown in figure 4.15.

For the campaign KNM6,  $\sigma_{\text{syst}}$  is clearly dominated by source-related effects, with the greatest impact by the column density (CD), followed by the energy loss function, plasma effects and the rear wall (RW). After KNM6, the impact of the CD decreases drastically by a factor of  $\sim \frac{1}{3}$  for KNM7 and another  $\sim 30\%$  for KNM8 and KNM9, respectively. The reason for this is the installation of a new e-gun after the campaign KNM6. This e-gun allows for a better CD determination with a smaller uncertainty (compare table 1 in the appendix). The described decrease of the CD impact after KNM6 makes the energy loss and plasma effects the leading systematics for KNM7 onwards. Also, the RW effects lose influence after the campaign KNM6 by a factor

---

<sup>10</sup>The upper and the lower uncertainty are averaged to obtain one value.

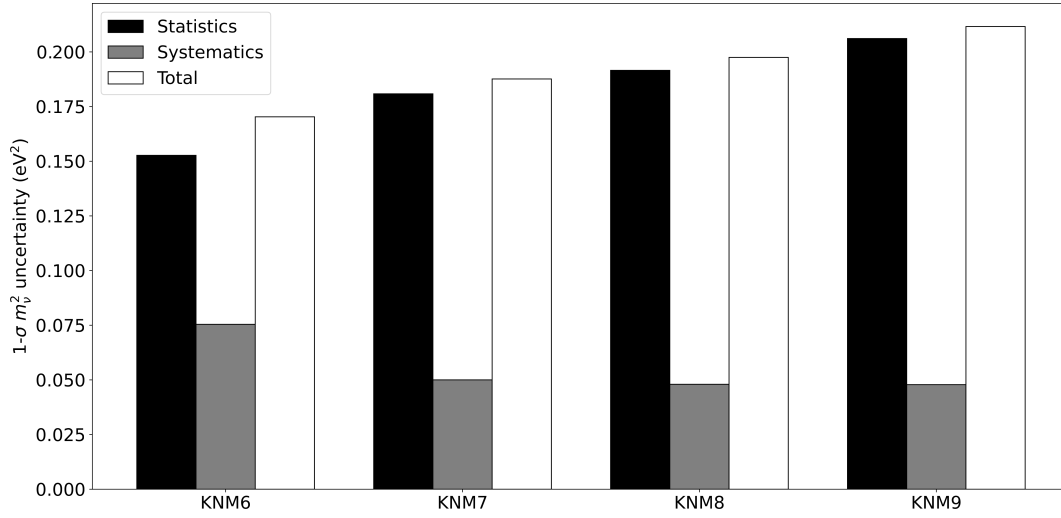


Figure 4.14: Statistical (black), systematic (grey) and total (white) uncertainty on the effective neutrino mass squared  $m_\nu^2$  for the campaigns KNM6-9, respectively.

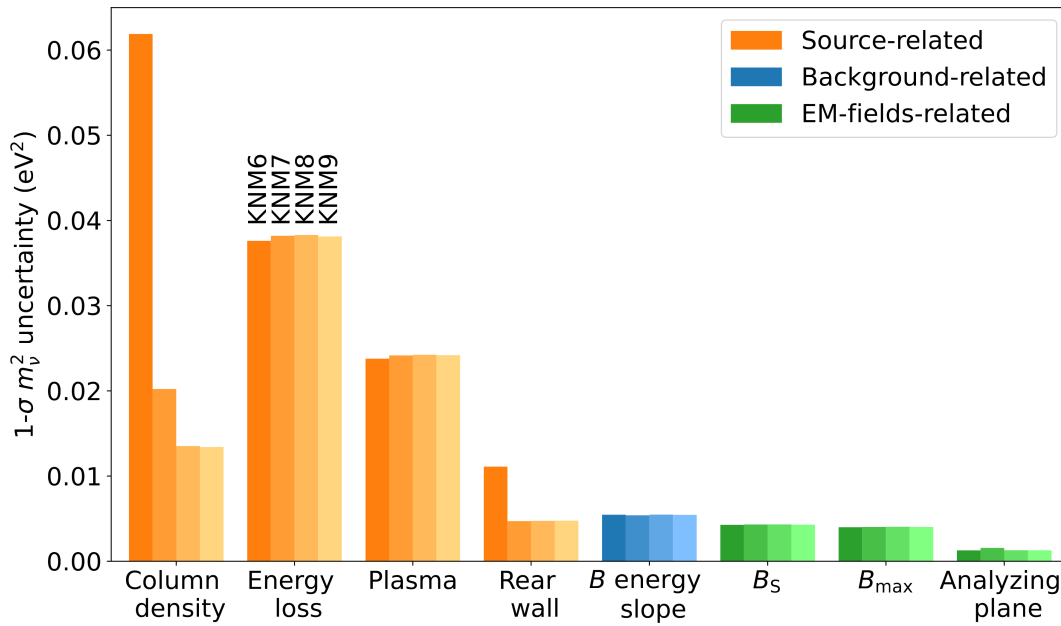


Figure 4.15: Systematics breakdowns for the campaigns KNM6-9, respectively. They show the influence of individual systematic effects on the total systematic uncertainty  $\sigma_{\text{sys}}$ . The decrease of the column density impact comes from the installation of an improved e-gun after the campaign KNM6. The reason for the rear wall decrease is a reduced rear wall activity since KNM7.

of  $\sim \frac{1}{2}$ . The RW impact for KNM7 onwards is lower than that for the background energy slope. The enlarged uncertainty for KNM6 comes from an increased RW activity, which leads to a background tritium spectrum, as described in section 2.3.1. The signal coming from the RW is approximately twice as high for KNM6 as for KNM7-9, respectively. The same holds for the uncertainties on this signal. The systematic effects related to the electromagnetic fields, namely the magnetic field of the source  $B_S$ , the maximum magnetic field  $B_{\max}$  and the effects regarding the analyzing plane, have the lowest influence for all campaigns, respectively.

All systematic effects, except the CD and the RW, have a constant impact on the total systematic uncertainty  $\sigma_{\text{syst}}$  over all four campaigns. There are multiple reasons for this:

- For the energy loss function, the background energy slope and the magnetic field of the source  $B_S$ , the same input parameter values and uncertainties are used for all four campaigns, respectively.
- For the source plasma, every effect explained in section 3.3.1 has the same input parameter values and uncertainties for all four campaigns, respectively, except the long-term fluctuation  $\sigma_{\text{long-term}}$ . The same placeholder values are used for KNM7-9, respectively. They differ from the ready KNM6 values as explained in section 4.2. For KNM6, the uncertainty of  $\sigma_{\text{long-term}}$  is one order of magnitude smaller than for KNM7-9, but this has nearly no influence ( $\mathcal{O}(10^{-5} \text{ eV}^2)$ ) on the overall plasma impact.
- For the maximum magnetic field  $B_{\max}$  and the effects regarding the analyzing plane, the input parameters and their uncertainties are different, but on the same order of magnitude.

In the following, an estimation of the total sensitivity on the effective neutrino mass  $m_\nu$  for the combination of the first nine KNM campaigns is made. The combined statistical uncertainty is

$$\sigma_{\text{stat},1-9} = \left( \sum_c \frac{1}{\sigma_{\text{stat},c}^2} \right)^{-\frac{1}{2}} = 0.07 \text{ eV}^2 \quad (4.2)$$

where the sum loops over all individual KNM campaigns (compare table 4.7). Because the determination of the combined systematic uncertainty is not trivial, an estimate for it has to be made. The source-related effects are dominating the total systematic uncertainty with an impact of  $\sim 0.036 \text{ eV}^2$  for the energy loss,  $\sim 0.023 \text{ eV}^2$  for the source plasma and a decreasing influence between  $0.062 \text{ eV}^2$  and  $0.013 \text{ eV}^2$  for the column density (compare figures 4.15 and 2.8). Since the other systematic effects are rather small, the combined systematic uncertainty is estimated

KNM campaign	$\sigma_{\text{stat}}$ (eV <sup>2</sup> )	$\sigma_{\text{syst}}$ (eV <sup>2</sup> )	$\sigma_{\text{tot}}$ (eV <sup>2</sup> )
1	0.809	0.268	0.852
2	0.307	0.171	0.352
3-NAP	0.568	0.285	0.636
3-SAP	0.561	0.270	0.622
4-NOM	0.231	0.129	0.264
4-OPT	0.293	0.080	0.304
5	0.170	0.073	0.185
6	0.153	0.075	0.170
7	0.181	0.050	0.188
8	0.192	0.048	0.197
9	0.206	0.048	0.212

Table 4.7: Statistical  $\sigma_{\text{stat}}$ , systematic  $\sigma_{\text{syst}}$  and total  $\sigma_{\text{tot}}$   $1\sigma$ -uncertainty on the effective neutrino mass squared  $m_\nu^2$  for the individual campaigns KNM1-9.

to  $\sigma_{\text{syst},1-9} = 0.06 \text{ eV}^2$ . The total uncertainty is then  $\sigma_{\text{tot},1-9} = 0.09 \text{ eV}^2$  (compare equation 4.1), which leads to a sensitivity on the effective electron anti-neutrino mass of  $m_\nu < 0.39 \text{ eV}$  (90 % C.L.). This brings the KATRIN experiment closer to its final goal.

As described in section 4.2, not all systematic input parameters used in the described analysis of the 6th to 9th KATRIN campaigns were ready by the time of this work. Furthermore, for the dominating source-related systematic effects, namely, the column density, the energy loss, and the source plasma, great and promising efforts have been made to decrease the individual impacts on the total systematic uncertainty. The improvement for the column density is already visible in figure 4.15. This will enhance the presented results even further.



# Chapter 5

## Conclusion and Outlook

The projected sensitivity of the KATRIN experiment on the effective electron anti-neutrino mass is  $m_\nu < 0.3 \text{ eV}$  (90% C.L.) after  $\sim 1000$  measurement days [25]. To achieve this, an efficient statistics collection is essential. As part of this thesis, the data monitoring tool *Webtrium* was successfully expanded. New plots allow to monitor the data taking efficiency and accumulation of statistics in almost real-time. This is meant to improve the statistics collection, which is a focus of the KATRIN measurement campaigns.

The latest KATRIN neutrino mass result with an upper limit of  $m_\nu < 0.45 \text{ eV}$  (90% C.L.) is based on the data of the first five measurement campaigns. A major part of this thesis was continuing the neutrino mass analysis of the following four KNM campaigns. A new data quality step was established as part of the run selection. A detailed inspection of the measurement time distribution (MTD), i.e. the actual retarding voltage set points and measurement times of each individual  $\beta$ -spectrum-scan, allows to spot outliers that could cause a neutrino mass bias. These investigations led to the rejection of one additional run from the KNM6 dataset and are now an integral part of the run selection procedure.

As the second part of the data selection process, the patch selection was carried out, which is the grouping of detector sections with similar transmission properties based on the pixel selection. For the campaign KNM6, the same 126 active pixels and patches as for the previous KNM5 dataset are used. The active pixels are grouped into 14 patches with 9 pixels each, using the pixel-wise middle of transmission values  $E_{1/2}$  as the sorting criterion. This procedure is not sufficient for the campaigns KNM7 and KNM8-9 because the number of active pixels reduced to 123 and 125, respectively, due to alignment changes in the KATRIN beamline. The patch selections presented in this thesis are based on these pixel selections and minimize the patch-wise variances  $\sigma_{E_{1/2}}^2$  across the 14 detector patches. In the future, the patch selection procedure will be optimized further to use fewer patches and reduce the computational costs of the analysis while not losing neutrino mass sensitivity.

After the data selection, the data quality and stability of the new neutrino mass data was studied. The three fit parameters, namely the endpoint energy  $E_0$ , the normalization factor  $A$  and the background rate  $B$  were examined regarding their

temporal and radial stability utilizing so-called run- and patch-wise fits. For  $E_0$ , indications for a time-wise drift for every campaign were visible, which can be explained by RW bias voltage adjustments and long-term source potential instabilities. This effect is considered in the neutrino mass analysis.  $A$  and  $B$  showed the expected constant behaviour over time. Also, the radial evolution of all three fit parameters was not unusual. Another part of the data quality investigations was the study of possible fit parameter dependencies on the different scanning directions, i.e. the high voltage ramping sequences of the KATRIN spectrometer. The presented results were consistent with the stability examinations and showed no significant patterns.

The last part of this thesis was a first sensitivity analysis of the campaigns KNM6-9. This analysis partially used non-final input parameters, so-called placeholders, and was carried out on simulated data, so-called twins. This is one part of the KATRIN blinding strategy. The data is only analyzed once all input parameters are finalized. With the presented analysis, the total sensitivity on  $m_\nu^2$  for the campaigns KNM6-9, respectively, could be determined. The dominating statistical  $1\text{-}\sigma$  uncertainties lie between  $0.153$  and  $0.206\text{ eV}^2$  and the systematic uncertainties range from  $0.048$  to  $0.075\text{ eV}^2$  for the four campaigns. With the so-called systematics breakdowns, a more detailed look at the impact of the individual systematic effects was possible. These investigations showed the decreasing influence of the column density and the rear wall on the total systematic uncertainty and also the unaltered impact of the other systematic effects, namely the energy loss, the source plasma, the background energy slope, the magnetic field of the source, the maximum magnetic field and the effects regarding the analyzing plane. The dominant systematic uncertainties are related to the column density, the energy loss function and the source plasma, which are the subject of ongoing works within the KATRIN collaboration.

As an outlook, the total combined sensitivity on the effective electron anti-neutrino mass  $m_\nu$  for all nine KNM campaigns was estimated. The obtained sensitivity of  $m_\nu < 0.39\text{ eV}$  (90% C.L.) brings the KATRIN experiment closer to its final goal.

## Bibliography

- [1] W. Pauli. »Pauli letter collection: letter to Lise Meitner«. URL: <https://cds.cern.ch/record/83282>.
- [2] C. L. Cowan et al. »Detection of the Free Neutrino: a Confirmation«. In: *Science* 124.3212 (1956), pp. 103–104. DOI: 10.1126/science.124.3212.103.
- [3] B. Povh et al. »Teilchen und Kerne: Eine Einführung in die physikalischen Konzepte«. Springer Berlin Heidelberg, 2013. URL: <https://books.google.de/books?id=QNgobAAAQBAJ>.
- [4] G. Danby et al. »Observation of High-Energy Neutrino Reactions and the Existence of Two Kinds of Neutrinos«. In: *Phys. Rev. Lett.* 9 (1 1962), pp. 36–44. DOI: 10.1103/PhysRevLett.9.36.
- [5] K. Kodama et al. »Observation of tau neutrino interactions«. In: *Physics Letters B* 504.3 (2001), pp. 218–224. DOI: [https://doi.org/10.1016/S0370-2693\(01\)00307-0](https://doi.org/10.1016/S0370-2693(01)00307-0).
- [6] Y. Fukuda et al. »Evidence for Oscillation of Atmospheric Neutrinos«. In: *Phys. Rev. Lett.* 81 (8 1998), pp. 1562–1567. DOI: 10.1103/PhysRevLett.81.1562.
- [7] Q. R. Ahmad et al. »Direct Evidence for Neutrino Flavor Transformation from Neutral-Current Interactions in the Sudbury Neutrino Observatory«. In: *Phys. Rev. Lett.* 89 (1 2002), p. 011301. DOI: 10.1103/PhysRevLett.89.011301.
- [8] J. N. Bahcall and R. Davis. »Solar Neutrinos: A Scientific Puzzle«. In: *Science* 191.4224 (1976), pp. 264–267. DOI: 10.1126/science.191.4224.264.
- [9] J. N. Bahcall and R. L. Sears. »Solar Neutrinos«. In: *Annual Review of Astronomy and Astrophysics* 10 (1972), pp. 25–44. DOI: 10.1146/annurev.aa.10.090172.000325.
- [10] Y. Fukuda et al. »Study of the atmospheric neutrino flux in the multi-GeV energy range«. In: *Physics Letters B* 436.1 (1998), pp. 33–41. DOI: [doi.org/10.1016/S0370-2693\(98\)00876-4](https://doi.org/10.1016/S0370-2693(98)00876-4).
- [11] B. Pontecorvo. »Mesonium and anti-mesonium«. In: *Sov. Phys. JETP* 6 (1957), p. 429.
- [12] B. Pontecorvo. »Inverse beta processes and nonconservation of lepton charge«. In: *Zh. Eksp. Teor. Fiz.* 34 (1957), p. 247.

- [13] Z. Maki, M. Nakagawa and S. Sakata. »Remarks on the Unified Model of Elementary Particles«. In: *Progress of Theoretical Physics* 28.5 (1962), pp. 870–880. DOI: [10.1143/PTP.28.870](https://doi.org/10.1143/PTP.28.870).
- [14] C. Giganti, S. Lavignac and M. Zito. »Neutrino oscillations: The rise of the PMNS paradigm«. In: *Progress in Particle and Nuclear Physics* 98 (2018), pp. 1–54. DOI: <https://doi.org/10.1016/j.ppnp.2017.10.001>.
- [15] J. Lesgourgues and S. Pastor. »Neutrino Mass from Cosmology«. In: *Advances in High Energy Physics* 2012.1 (2012), p. 608515. DOI: <https://doi.org/10.1155/2012/608515>.
- [16] P. D. Group et al. »Review of Particle Physics«. In: *Progress of Theoretical and Experimental Physics* 2022.8 (2022), p. 083C01. DOI: [10.1093/ptep/ptac097](https://doi.org/10.1093/ptep/ptac097).
- [17] A. G. Adame et al. »DESI 2024 VI: Cosmological Constraints from the Measurements of Baryon Acoustic Oscillations«. 2024. arXiv: 2404.03002 [astro-ph.CO].
- [18] Aghanim, N. et al. »Planck 2018 results - VI. Cosmological parameters«. In: *A&A* 641 (2020), A6. DOI: [10.1051/0004-6361/201833910](https://doi.org/10.1051/0004-6361/201833910).
- [19] S. R. Elliott and P. Vogel. »DOUBLE BETA DECAY«. In: *Annual Review of Nuclear and Particle Science* 52. Volume 52, 2002 (2002), pp. 115–151. DOI: [10.1146/annurev.nucl.52.050102.090641](https://doi.org/10.1146/annurev.nucl.52.050102.090641).
- [20] M. Agostini et al. »Final Results of GERDA on the Search for Neutrinoless Double- $\beta$  Decay«. In: *Phys. Rev. Lett.* 125 (25 2020), p. 252502. DOI: [10.1103/PhysRevLett.125.252502](https://doi.org/10.1103/PhysRevLett.125.252502).
- [21] D. Q. Adams et al. »With or without  $\nu$ ? Hunting for the seed of the matter-antimatter asymmetry«. 2024. arXiv: 2404.04453 [nucl-ex].
- [22] S. Abe et al. »Search for Majorana Neutrinos with the Complete KamLAND-Zen Dataset«. In: (2024). arXiv: 2406.11438 [hep-ex].
- [23] E. W. Otten and C. Weinheimer. »Neutrino mass limit from tritium  $\beta$  decay«. In: *Reports on Progress in Physics* 71.8 (2008), p. 086201. DOI: [10.1088/0034-4885/71/8/086201](https://doi.org/10.1088/0034-4885/71/8/086201).
- [24] URL: <https://www.katrin.kit.edu/> (visited on 17/06/2024).
- [25] M. Aker et al. »Direct neutrino-mass measurement based on 259 days of KATRIN data«. 2024. arXiv: 2406.13516.
- [26] URL: <https://www.kit.edu/> (visited on 18/06/2024).
- [27] URL: <https://www.iap.kit.edu/tlk/english/index.php> (visited on 27/06/2024).

- [28] M. Aker et al. »The design, construction, and commissioning of the KATRIN experiment«. In: *Journal of Instrumentation* 16.08 (2021), T08015. DOI: 10.1088/1748-0221/16/08/T08015.
- [29] C. Kraus et al. »Final results from phase II of the Mainz neutrino mass search in tritium  $\beta$  decay«. In: *The European Physical Journal C* 40.4 (2005), pp. 447–468. DOI: 10.1140/epjc/s2005-02139-7.
- [30] V. N. Aseev et al. »Upper limit on the electron antineutrino mass from the Troitsk experiment«. In: *Phys. Rev. D* 84 (11 2011), p. 112003. DOI: 10.1103/PhysRevD.84.112003.
- [31] M. Kleesiek et al. » $\beta$ -Decay spectrum, response function and statistical model for neutrino mass measurements with the KATRIN experiment«. In: *The European Physical Journal C* 79.3 (2019). DOI: 10.1140/epjc/s10052-019-6686-7.
- [32] M. Aker et al. »Analysis methods for the first KATRIN neutrino-mass measurement«. In: *Phys. Rev. D* 104 (1 2021), p. 012005. DOI: 10.1103/PhysRevD.104.012005.
- [33] R. B. Firestone and V. S. Shirley. »Table of Isotopes«. 8th Edition. John Wiley & Sons, Inc., 2005. URL: <https://www.wiley-vch.de/de/fachgebiete/naturwissenschaften/table-of-isotopes-978-0-471-35633-2>.
- [34] C. R. Karl. »First Sub-Electronvolt Direct Neutrino Mass Measurement with the KATRIN Experiment«. en. Technische Universität München, 2022, p. 165. URL: <https://mediatum.ub.tum.de/1659153>.
- [35] O. Kazachenko et al. »Tritium Processing Loop for KATRIN Experiment«. In: *Fusion Science and Technology* 54.1 (2008), pp. 67–70. DOI: 10.13182/FST08-A1766.
- [36] V. Lobashev and P. Spivak. »A method for measuring the electron antineutrino rest mass«. In: *Nuclear Instruments and Methods in Physics Research Section A: Accelerators, Spectrometers, Detectors and Associated Equipment* 240.2 (1985), pp. 305–310. DOI: 10.1016/0168-9002(85)90640-0.
- [37] A. Picard et al. »A solenoid retarding spectrometer with high resolution and transmission for keV electrons«. In: *Nuclear Instruments and Methods in Physics Research Section B: Beam Interactions with Materials and Atoms* 63.3 (1992), pp. 345–358. DOI: 10.1016/0168-583X(92)95119-C.
- [38] G. Beamson, H. Q. Porter and D. W. Turner. »The collimating and magnifying properties of a superconducting field photoelectron spectrometer«. In: *Journal of Physics E: Scientific Instruments* 13.1 (1980), p. 64. DOI: 10.1088/0022-3735/13/1/018.

- [39] J. Amsbaugh et al. »Focal-plane detector system for the KATRIN experiment«. In: *Nuclear Instruments and Methods in Physics Research Section A: Accelerators, Spectrometers, Detectors and Associated Equipment* 778 (2015), pp. 40–60. DOI: 10.1016/j.nima.2014.12.116.
- [40] S. Schneidewind et al. »Improved treatment of the  $T_2$  molecular final-states uncertainties for the KATRIN neutrino-mass measurement«. In: *Eur. Phys. J. C* 84.5 (2024), p. 494. DOI: 10.1140/epjc/s10052-024-12802-w.
- [41] V. Hannen et al. »Deconvolution of the energy loss function of the KATRIN experiment«. In: *Astroparticle Physics* 89 (2017), pp. 30–38. DOI: 10.1016/j.astropartphys.2017.01.010.
- [42] J. W. Liu. »Total cross sections for high-energy electron scattering by  $H_2$  ( $^1\Sigma_g^+$ ),  $N_2$  ( $^1\Sigma_g^+$ ), and  $O_2$  ( $^3\Sigma_g^-$ )«. In: *Phys. Rev. A* 35 (2 1987), pp. 591–597. DOI: 10.1103/PhysRevA.35.591.
- [43] V. Aseev et al. »Energy loss of 18 keV electrons in gaseous T and quench condensed D films«. In: *The European Physical Journal D* 10 (2000), pp. 39–52. DOI: 10.1007/s100530050525.
- [44] M. Aker et al. »Precision measurement of the electron energy-loss function in tritium and deuterium gas for the KATRIN experiment«. In: *The European Physical Journal C* 81.7 (2021). DOI: 10.1140/epjc/s10052-021-09325-z.
- [45] Y.-K. Kim, J. P. Santos and F. Parente. »Extension of the binary-encounter-dipole model to relativistic incident electrons«. In: *Phys. Rev. A* 62 (5 2000), p. 052710. DOI: 10.1103/PhysRevA.62.052710.
- [46] M. Kleesiek. »A Data-Analysis and Sensitivity-Optimization Framework for the KATRIN Experiment«. Karlsruhe Institut für Technologie (KIT), 2014. DOI: 10.5445/IR/1000043301.
- [47] M. B. Machatschek. »A Phenomenological Theory of KATRIN Source Potential Systematics and its Application in Krypton-83m Calibration Measurements«. Karlsruhe Institut für Technologie (KIT), 2021. DOI: 10.5445/IR/1000132391.
- [48] M. Aker et al. »In Situ Tritium Decontamination of the KATRIN Rear Wall Using an Ultraviolet/Ozone Treatment«. In: *Fusion Science and Technology* 80.3-4 (2024), pp. 303–310. DOI: 10.1080/15361055.2023.2214695.
- [49] A. K. Schaller. »Characterization and mitigation of the background in KATRIN«. en. Technische Universität München, 2020, p. 174. URL: <https://mediatum.ub.tum.de/1553598>.
- [50] F. Block. »Determination of Electromagnetic Fields and Tritium Column Density for Neutrino Mass Analysis with KATRIN«. Karlsruhe Institut für Technologie (KIT), 2022. DOI: 10.5445/IR/1000145073.

- [51] K. Valerius. »Spectrometer-related background processes and their suppression in the KATRIN experiment«. Munster U., 2009.
- [52] F. M. Fränkle et al. »Penning discharge in the KATRIN pre-spectrometer«. In: *Journal of Instrumentation* 9.07 (2014), P07028. DOI: 10.1088/1748-0221/9/07/P07028.
- [53] M. Aker et al. »Suppression of Penning discharges between the KATRIN spectrometers«. In: *The European Physical Journal C* 80.9 (2020). DOI: 10.1140/epjc/s10052-020-8278-y.
- [54] S. Mertens et al. »Background due to stored electrons following nuclear decays in the KATRIN spectrometers and its impact on the neutrino mass sensitivity«. In: *Astroparticle Physics* 41 (2013), pp. 52–62. DOI: 10.1016/j.astropartphys.2012.10.005.
- [55] A. Lokhov et al. »Background reduction at the KATRIN experiment by the shifted analysing plane configuration«. In: *Eur. Phys. J. C* 82.3 (2022), p. 258. DOI: 10.1140/epjc/s10052-022-10220-4.
- [56] G. Cowan. »Statistical Data Analysis«. Oxford University Press, 1998. DOI: 10.1093/oso/9780198501565.001.0001.
- [57] S. S. Wilks. »The Large-Sample Distribution of the Likelihood Ratio for Testing Composite Hypotheses«. In: *The Annals of Mathematical Statistics* 9.1 (1938), pp. 60–62. DOI: 10.1214/aoms/1177732360.
- [58] C. Karl. »Analysis of First Tritium Data of the KATRIN Experiment«. Technische Universität München, 2018.
- [59] M. Arenz et al. »Calibration of high voltages at the ppm level by the difference of  $^{83\text{m}}\text{Kr}$  conversion electron lines at the KATRIN experiment«. In: *The European Physical Journal C* 78.5 (2018). DOI: 10.1140/epjc/s10052-018-5832-y.
- [60] M. Erhard et al. »High-voltage monitoring with a solenoid retarding spectrometer at the KATRIN experiment«. In: *Journal of Instrumentation* 9.06 (2014), P06022. DOI: 10.1088/1748-0221/9/06/P06022.
- [61] T. Thümmeler, R. Marx and C. Weinheimer. »Precision high voltage divider for the KATRIN experiment«. In: *New Journal of Physics* 11.10 (2009), p. 103007. DOI: 10.1088/1367-2630/11/10/103007.
- [62] C. Karl, P. Eller and S. Mertens. »Fast and precise model calculation for KATRIN using a neural network«. English. In: *European Physical Journal C* 82.5 (2022). DOI: 10.1140/epjc/s10052-022-10384-z.

- [63] A. Owen. »The Unreasonable Effectiveness of Quasirandom Sequences«. URL: <https://extremelearning.com.au/unreasonable-effectiveness-of-quasirandom-sequences/> (visited on 21/08/2024).
- [64] M. Aker et al. »Measurement of the electric potential and the magnetic field in the shifted analysing plane of the KATRIN experiment«. 2024. arXiv: 2408.07022 [physics.ins-det].
- [65] F. Fränkle et al. »Golden Pixel selection KNM1-5«. KATRIN internal. URL: [https://iap-katrin-wiki.iap.kit.edu/katrin/images/8/89/Golden\\_Pixel\\_Selection\\_KNM1\\_5.pdf](https://iap-katrin-wiki.iap.kit.edu/katrin/images/8/89/Golden_Pixel_Selection_KNM1_5.pdf) (visited on 01/09/2024).
- [66] M. Slezák. »Monitoring of the energy scale in the KATRIN neutrino experiment«. Charles University in Prague, 2015. URL: [http://www.katrin.kit.edu/publikationen/phd-Martin\\_Slezak.pdf](http://www.katrin.kit.edu/publikationen/phd-Martin_Slezak.pdf).
- [67] K. Schönung. »Development of a Rear Wall for the KATRIN Rear Section and investigation of tritium compatibility of Rear Section components«. Karlsruhe Institut für Technologie (KIT), 2016. DOI: 10.5445/IR/1000056077.
- [68] L. Köllenberger. »KNM1-5 ENDPOINT SHIFTS AND DRIFTS«. KATRIN internal. URL: [https://iap-katrin-wiki.iap.kit.edu/katrin/images/d/d3/TechReport-endpointDrifts\\_KNM1-5.pdf](https://iap-katrin-wiki.iap.kit.edu/katrin/images/d/d3/TechReport-endpointDrifts_KNM1-5.pdf) (visited on 01/09/2024).
- [69] B. Efron. »Bootstrap Methods: Another Look at the Jackknife«. In: *The Annals of Statistics* 7.1 (1979), pp. 1–26. DOI: 10.1214/aos/1176344552.

# Appendix

## Detailed systematic input parameter values

KNM campaign	6	7	8	9
Column density $\rho d$ ( $10^{21}/\text{m}^2$ )	$3.730 \pm 0.037$	$3.750 \pm 0.011$	$3.750 \pm 0.008$	$3.750 \pm 0.008$
Plasma potential broadening $\sigma_z^2$ ( $10^{-3} \text{ eV}^2$ )	$0.89 \pm 0.19$	$0.89 \pm 0.19$	$0.89 \pm 0.19$	$0.89 \pm 0.19$
Plasma long-term fluctuations $\sigma_{\text{long-term}}^2$ ( $10^{-3} \text{ eV}^2$ )	$0.15 \pm 0.08$	$0.00 \pm 1.00$	$0.00 \pm 1.00$	$0.00 \pm 1.00$
Rear wall endpoint $E_{0,\text{RW}}$ (eV)	$18576.5 \pm 0.5$	$18576.5 \pm 0.5$	$18576.5 \pm 0.5$	$18576.5 \pm 0.5$
Background energy slope $m_B$ ( $10^{-9} \text{ cps}/(\text{eV} \cdot \text{pixel})$ )	$9 \pm 6$	$9 \pm 6$	$9 \pm 6$	$9 \pm 6$
Magnetic field of the source $B_S$ (T)	$2.507 \pm 0.006$	$2.507 \pm 0.006$	$2.507 \pm 0.006$	$2.507 \pm 0.006$

Table 1: Selection of input values for systematic effects with uncertainties used for the neutrino mass analysis in this thesis for the campaigns KNM6-9.

## Time-wise overdispersion values

KNM campaign	6	7	8	9
Overdispersion of $A$ ( $10^{-6}$ )	$-5 \pm 11$	$-9 \pm 14$	$-22 \pm 13$	$5 \pm 13$
Overdispersion of $B$ (mcps <sup>2</sup> )	$-1.9 \pm 2.0$	$1.8 \pm 2.6$	$3.8 \pm 2.8$	$-0.5 \pm 2.6$

Table 2: Overdispersion values of the run-wise normalization factor  $A$  and the background rate  $B$  for the campaigns KNM6-9, respectively. The quoted uncertainties are determined via the bootstrapping method [69].

## Patch-wise fits

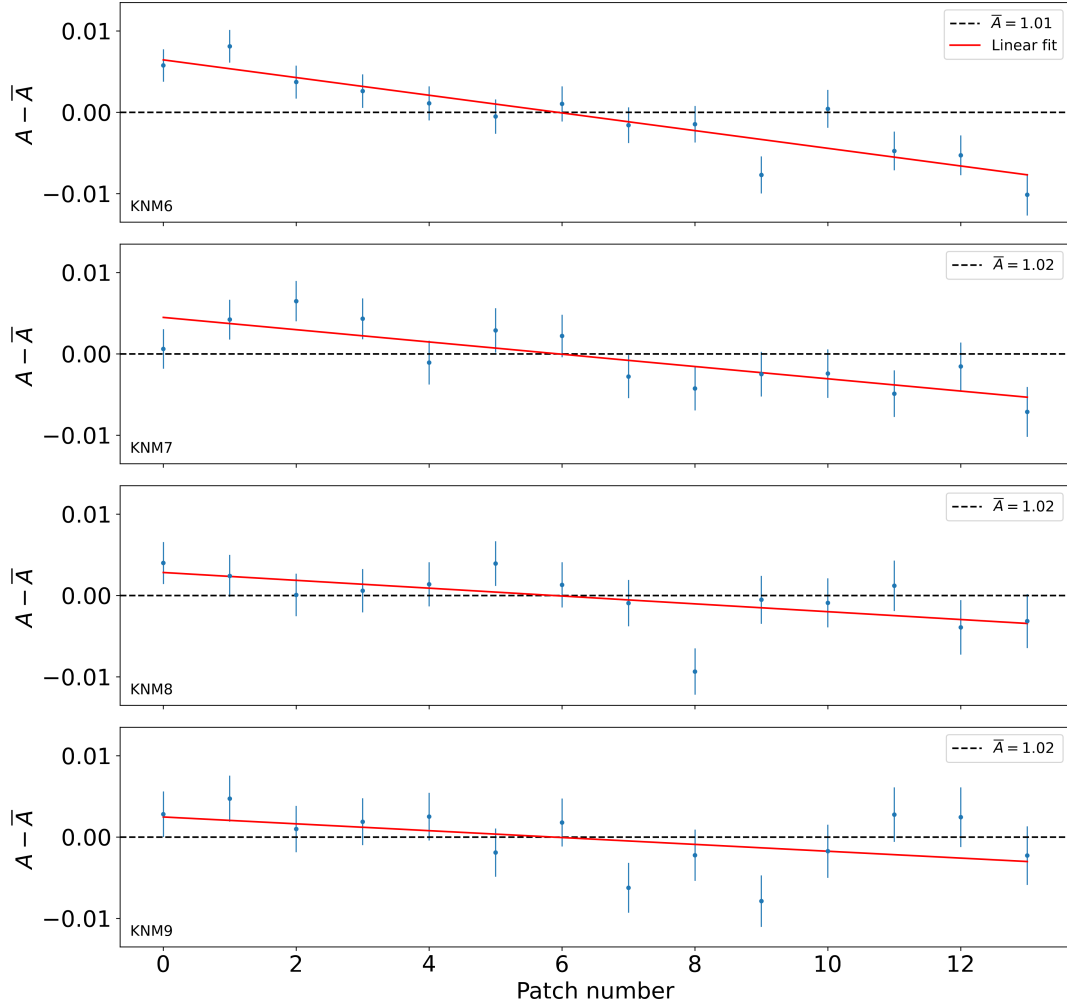


Figure 1: Patch-wise evolution of the normalization factor  $A$  for the campaigns KNM6-9, respectively. All runs of a campaign are stacked, and every detector patch is fitted individually, with statistical uncertainty only. The effective neutrino mass is fixed to zero ( $m_\nu = 0$  eV). A linear fit (red) to the blue parameter values is performed for every campaign, respectively.

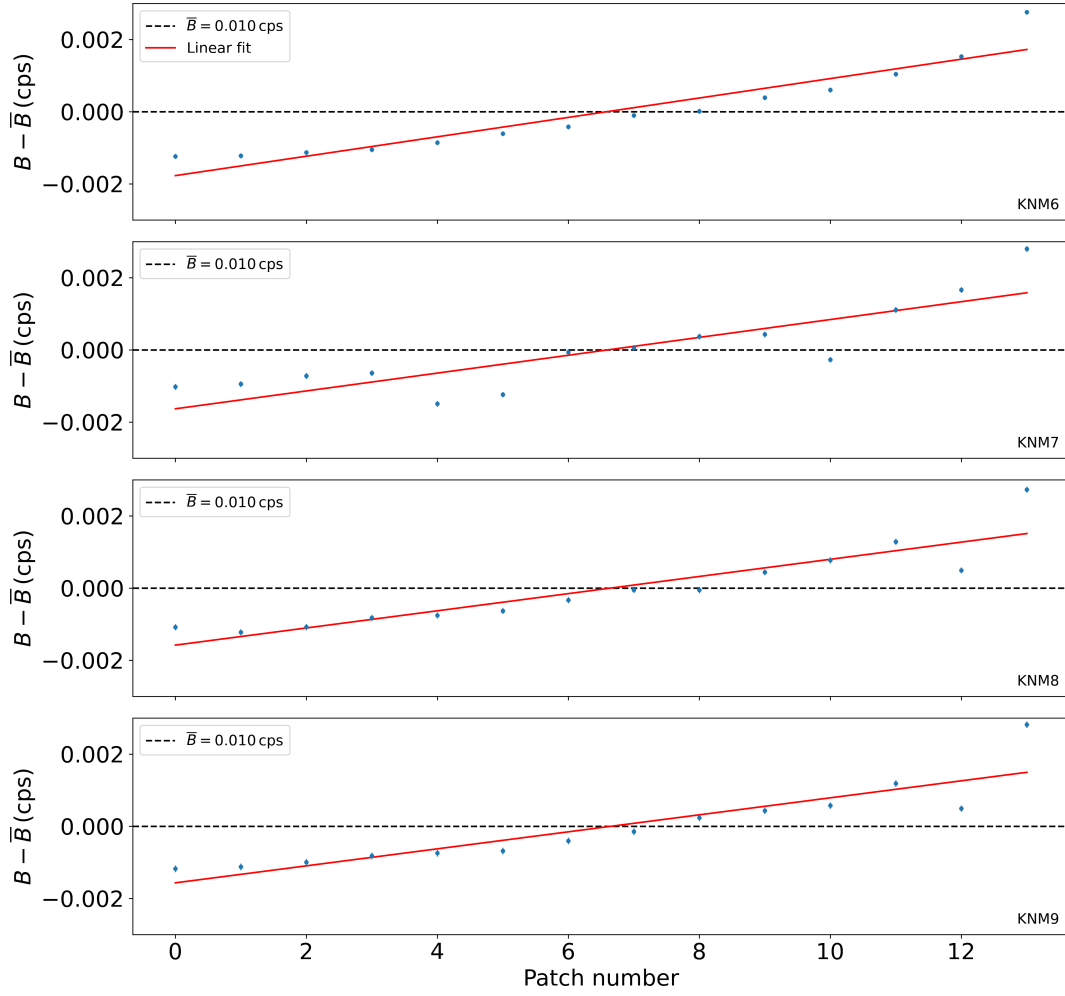


Figure 2: Patch-wise evolution of the background rate  $B$  for the campaigns KNM6-9, respectively. All runs of a campaign are stacked, and every detector patch is fitted individually, with statistical uncertainty only. The effective neutrino mass is fixed to zero ( $m_\nu = 0$  eV). A linear fit (red) to the blue parameter values is performed for every campaign, respectively.

## Patch-wise slope values

KNM campaign	6	7	8	9
Linear slope of $A$ ( $10^{-3}$ /patch)	$-1.09 \pm 0.10$	$-0.75 \pm 0.13$	$-0.48 \pm 0.14$	$-0.42 \pm 0.15$
Linear slope of $B$ (mcps/patch)	$0.269 \pm 0.003$	$0.247 \pm 0.004$	$0.238 \pm 0.004$	$0.236 \pm 0.004$

Table 3: Values of the linear slopes, fitted to the patch-wise normalization factor  $A$  and background rate  $B$  fit values, for the campaigns KNM6-9, respectively.

## Scanning direction dependency

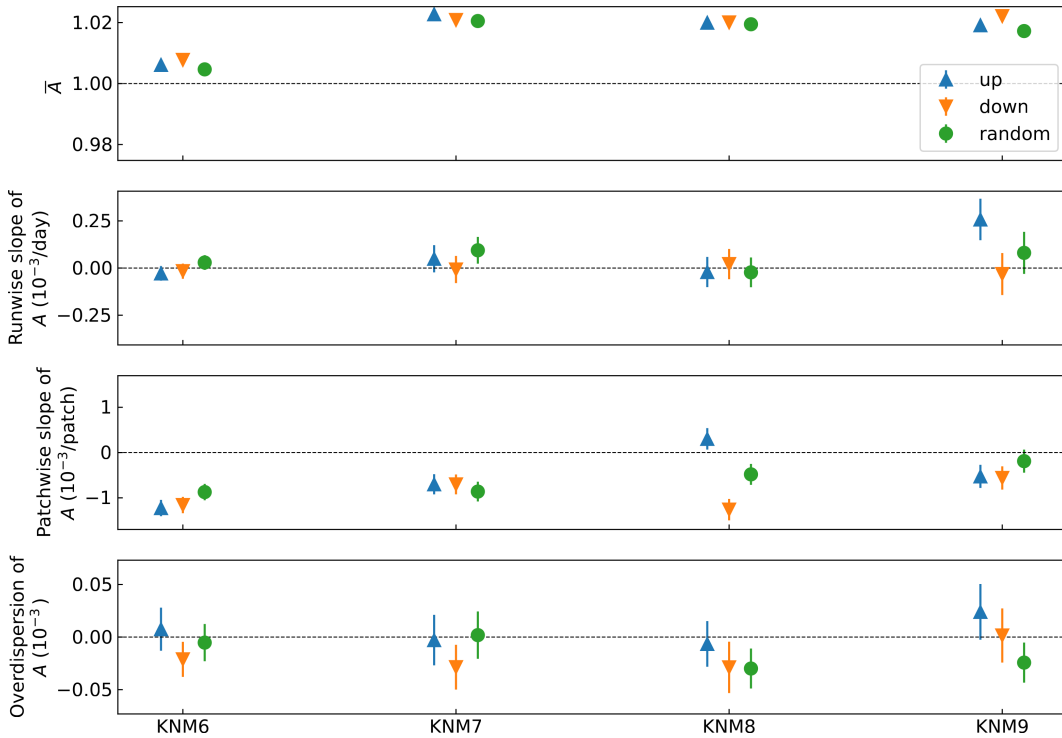


Figure 3: Results of the data quality investigations for the normalization factor  $A$ , regarding the dependency of the fit parameters on different scanning directions of the retarding voltage  $U$ .

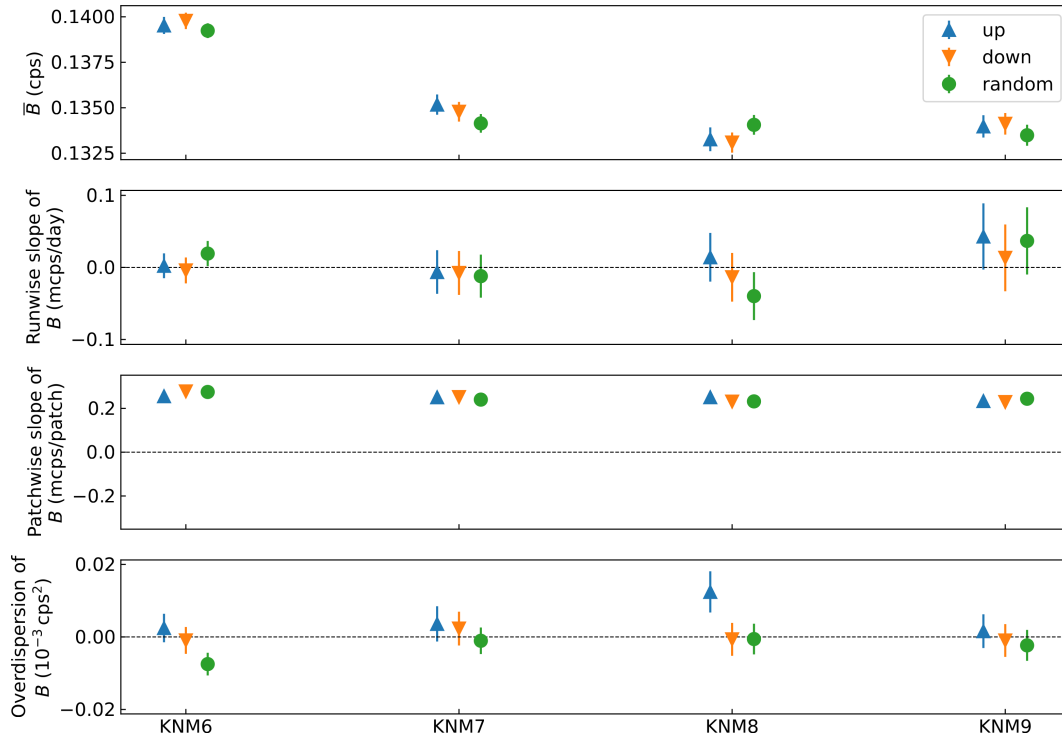


Figure 4: Results of the data quality investigations for the background rate  $B$ , regarding the dependency of the fit parameters on different scanning directions of the retarding voltage  $U$ .



# Acknowledgements

I want to thank everyone who supported me during the work of this thesis, in particular

- Prof. Dr. Susanne Mertens for the chance to work in the KATRIN collaboration on this exciting project,
- Dr. Christoph Wiesinger for his continuous support and advice throughout this thesis,
- Xaver Stribl and Alessandro Schwemmer as the best office-mates in the coolest office in town for all their help during my work and all the fun we had in our office,
- Matthias Meier for all the funny breaks during work and his flipping tips,
- all members of the KATRIN team, also including Christoph Köhler, for the great time we had during collaboration meetings, analysis workshops and measurement shifts,
- everyone who proof-read parts of this thesis
- and all members of our group E47 for the extraordinary working environment and all the amusing social activities.

Ganz zum Schluss möchte ich mich bei meinen Eltern, meinem Bruder, meiner Freundin und all meinen Freunden bedanken, die mich immer bedingungslos unterstützt haben und ohne die diese Arbeit und dieses ganze Studium nicht möglich gewesen wären.